Supplement of Clim. Past, 21, 571–592, 2025
https://doi.org/10.5194/cp-21-571-2025-supplement

Supplement of

Sediment fluxes dominate glacial–interglacial changes in ocean carbon inventory: results from factorial simulations over the past 780 000 years

Markus Adloff et al.

Correspondence to: Markus Adloff (markus.adloff@unibe.ch)

Supplementary Information for Adloff et al. 2024

S1. Physical model parameterisations

The geostrophic-frictional balance ocean circulation is calculated explicitly (Edwards et al., 1998; Müller et al., 2006), and parameterizations are included to represent the effects of dia- and isopycnal diffusion and eddy-induced transport (Griffies, 1998). The NCEP/NCAR monthly wind stress climatology (Kalnay et al., 1996) is used to prescribe wind stress at the ocean surface. Atmosphere-ocean gas exchange and carbonate chemistry are simulated according to the OCMIP-2 protocols (Najjar et al., 1999; Orr et al., 1999, 2017; Wanninkhof, 2014; Orr and Epitalon, 2015), and gas transfer velocities are linearly scaled with wind speed instead to quadratic (Krakauer et al., 2006). The global mean sea-air gas exchange was then reduced by 19% to achieve agreement with pre-bomb testing radiocarbon distribution estimates and 20th century observations (Müller et al., 2008). This is a standard adjustment in Bern3D and accounts for the fact that Δ14C in the surface ocean is overestimated by the gas transfer velocities calculated from wind speed.

S2. Model limitations

There are several ways in which the amplitude or regional pattern of the simulated changes might be biased by our experiment design. Firstly, by design our forcings are smooth in time and spatially uniform, which is a stark simplification. For example, the PO4 forcing ties nutrient supply to the δ^{18}O record. The correlation between dust (iron source to the open ocean) concentrations in the EPICA Dome C ice core and benthic δ^{18}O is of first order only and varies over the glacial cycle (Winckler et al., 2008). Several macro- and micronutrients were likely supplied to varying parts of the glacial ocean (Broecker, 1982b; Martin, 1990; Pollock, 1997; Deutsch et al., 2004) and while dust flux changes seem to correlate globally (Kukla et al., 1990; Winckler et al., 2008), the timings and rates of other nutrient fluxes might in reality have varied temporally and spatially. Similarly, our other forcings might change more slowly over the deglaciation than the real processes they mimic. A more detailed analysis of non-linear interactions between the tested forcings would require an additional simulation ensemble that tests all possible forcing combinations and ideally also with varying forcing magnitudes.

Another simplification in our experiment design is that the majority of our simulations assume temporally constant terrestrial solute inputs although in reality these fluxes are climate sensitive (Munhoven, 2002). It is unlikely that removing this simplification would substantially alter the simulated global carbon fluxes and reservoir size changes because it is estimated that global weathering rate changes during glacial cycles were small despite large local variability, possibly because they canceled out in the global mean (Jones et al., 2002; Von Blanckenburg et al., 2015; Frings, 2019; Börker et al., 2020). It was estimated that glacial-interglacial weathering flux changes altered atmospheric CO_2 by a maximum of 20 ppm (Köhler and Munhoven, 2020). Yet, the resulting δ^{13}C perturbation could be larger because a global balance in carbon flux changes does not imply a balance in carbon isotope fluxes (Jeltsch-Thömmes and Joos, 2023). Additionally, there might have been non-linear changes in isotopic input fluxes during the simulated time period.

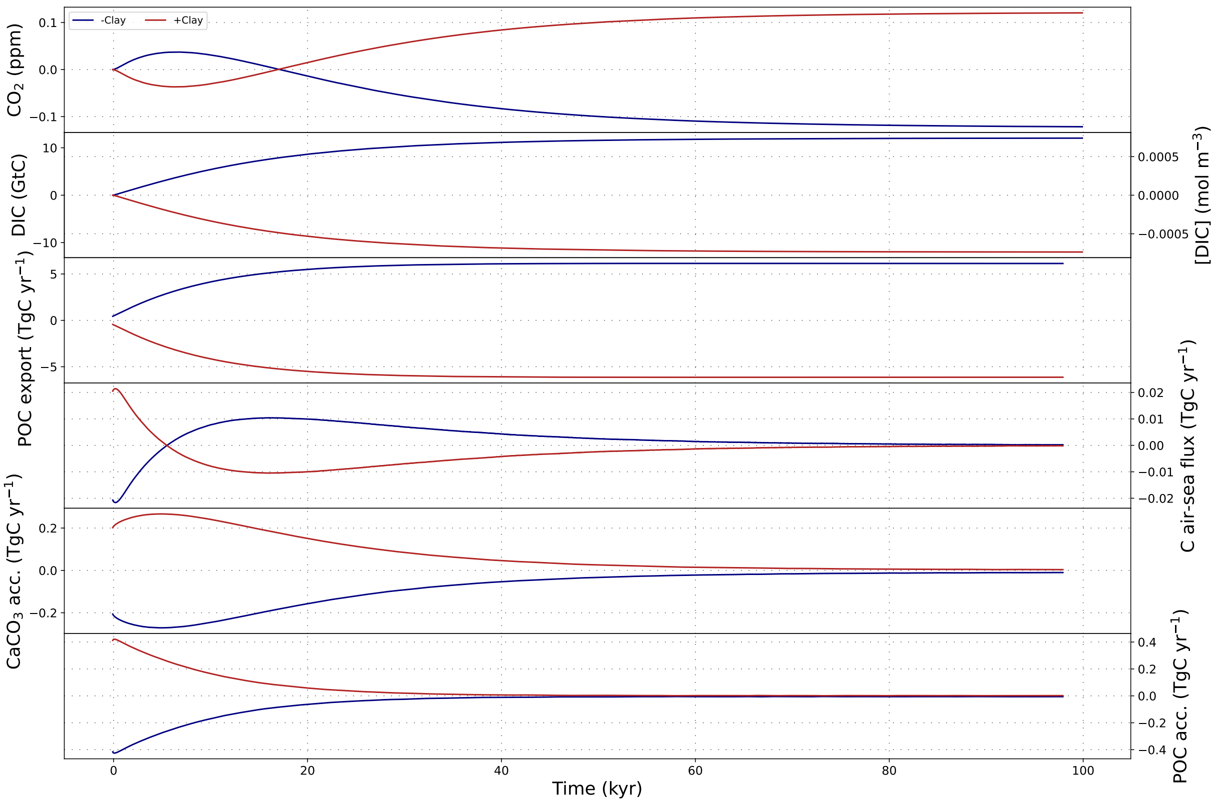

Figure S1. The effect of step changes of plus or minus 30% of the prescribed clay flux on atmospheric CO_2 concentrations, DIC and carbon fluxes over 100 kyr.

Finally, the imbalance between weathering and burial fluxes is also shaped by the sedimentation rate. In our simulations, sedimentation rates vary due to changes in biogenic export, yet accumulation of non-biogenic material was kept constant. This omission, however, is not a large error source, given that a separately prescribed step-wise 30% increase and decrease of the non-biogenic flux in the PI steady state had only marginal effects on atmospheric CO_2, DIC and sedimentary accumulation of biogenic particles (Fig. S1).

S3. Effects of orbital, insolation and albedo changes on carbon fluxes

In the following, we examine the underlying glacial-interglacial carbon cycle changes and the effect of interactive sediments under each forcing. First we focus on the standard forcing, before discussing the effects of additional forcings.

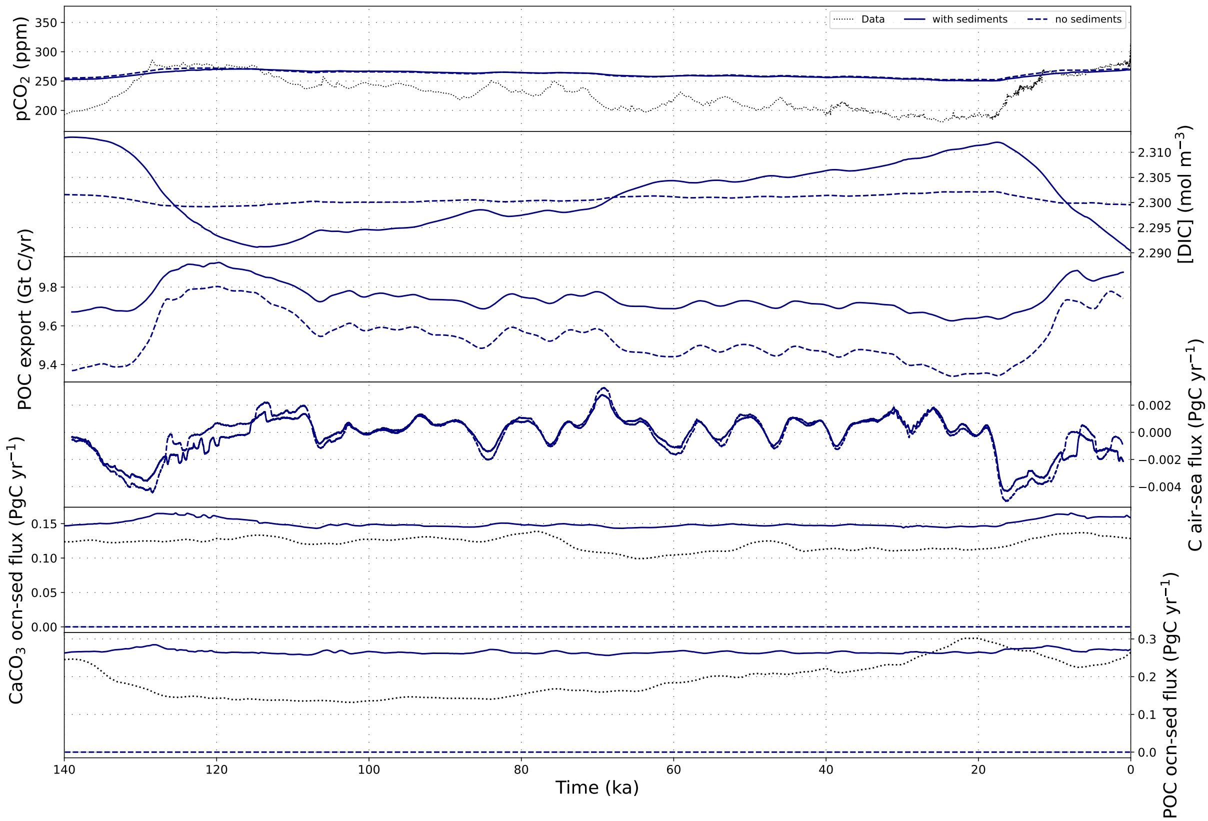

Figure S2. Atmospheric CO_2 concentrations, DIC and carbon fluxes over the most recent full glacial cyle in simulation BASE with and without dynamic sediments.

The dynamic circulation and climate affect the partitioning of carbon between the interactive carbon reservoirs in the model (atmosphere, ocean, reactive sediments and lithosphere). The applied forcings vary the CO_2 concentration gradient between air and seawater by modifying CO_2 solubility and surface ocean DIC and alkalinity concentrations. Without dynamic sediments (Fig S2), carbon in response moves between the atmosphere, the marine DIC and, to a lesser extent, DOC reservoirs in the ocean. With the standard forcing, CO_2 and O_2 solubilities increase during glacial phases because of the cooling surface ocean, leading to a steady marine uptake of carbon and oxygen from the atmosphere from peak interglacial through to the glacial maximum. The cooling reduces deep water formation rates in the North Atlantic and increases deep water formation in the Southern Ocean. These circulation changes increase the marine uptake of CO_2 while expanding sea ice prevents outgassing of marine CO_2 in the Southern Ocean. Overall POC and $CaCO_3$ export fluxes decrease during glaciation despite increased primary productivity in mid-latitudes and sub-tropics due to reduced export production in the high latitudes, predominantly due to sea ice growth, in places also because of reduced nutrient supply and lower temperatures. These export fluxes changes, particularly in the Southern Ocean, alter phosphate cycling: In interglacial states, high export fluxes effectively transfer phosphate from the photic zone to the intermediate ocean, where most exported POC is remineralized. Upwelling of intermediate water masses returns phosphate to the surface ocean. In glacial states, less of the phosphate upwelling in the Southern Ocean is incorporated into POC and exported to intermediate ocean depths. Instead, it is downwelled and incorporated into bottom waters. In consequence, the glacial deep ocean is enriched in preformed phosphate, while phosphate concentrations at intermediate depth decrease due to climate-driven export reduction. In the surface, reduced upwelling of nutrients and reduced nutrient uptake result in almost no net change of nutrient concentrations. During deglaciation, surface and deep waters warm and upwelling as well as export fluxes are restored. Hence, decreases in atmospheric CO_2 concentration during the onsets of glaciations are directly mirrored by increases in marine DIC and decreases in marine DOC, and the inverse occurs during deglaciation.

When interactive sediments are included in the simulations, export production and ocean chemistry changes alter sediment burial and dissolution fluxes, resulting in more than 10x larger DIC fluctuations over a glacial cycle than in the closed system. Changes in net sea-air gas exchange across the glacial cycle ($\sim$0.007 PgC/yr) are smaller than changes in each POC and $CaCO_3$ burial rates ($\sim$0.02 PgC/yr). $CaCO_3$ burial is predominantly driven by productivity changes and peaks during interglacials. In glacials, $CaCO_3$ burial is reduced below areas with reduced euphotic zone $CaCO_3$ export, e.g. in the high latitudes, but additionally where $CaCO_3$ becomes unstable due lower temperatures or reduced pH due to increased sedimentary POC oxydation rates. The standard forcing is not sufficient to cause wide-spread O_2 depletion in the glacial deep ocean, hence under the standard forcing POC burial rates are driven by export production rates, with less/more burial in areas with reduced/increased POC export production, respectively. The exception is the upwelling zone in the Equatorial East Pacific and parts of the Indian Ocean, where increased POC export depletes benthic and sediment pore water O_2 during glacial phases. During deglaciations, sea ice recedes, ocean ventilation increases and the surface and intermediate oceans warm, fostering increased primary productivity. While productivity and POC burial increase quickly in the subpolar regions, POC burial rates in the Eastern Equatorial Pacific respond more slowly to the warming: Long turnover timescales of pore water O_2 in sediments and remineralisation of previously deposited POC delay the return of interglacial POC remineralisation rates relative to export rates from the surface ocean. Therefore, deglaciations are marked by faster productivity increases in the surface ocean than sedimentary POC remineralisation. This results in a 'sweet spot' during glacial terminations, when tropical POC burial is still higher than in the interglacial while extratropical POC export and burial has already recovered to interglacial levels, particularly during the last 400 kyr which show larger glacial-interglacial temperature contrasts and faster warming rates during deglaciations. This 'sweet spot' causes the maximum of global POC burial to occur during deglaciation, before the full interglacial.

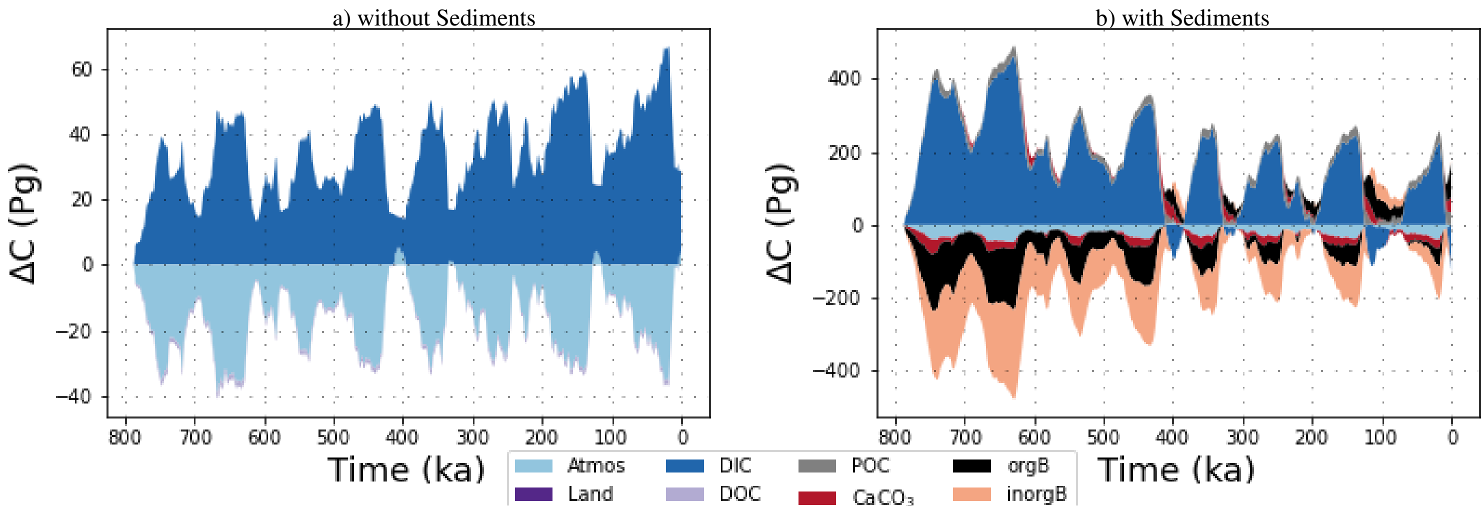

Figure S3. Transient carbon reservoir size changes across the last 780kyr as simulated in simulations with the standard (orbital, radiation and albedo) forcings in simulation BASE with and without dynamic marine sediments. Shown are the size changes of atmospheric, terrestrial, marine (DIC and DOC), sedimentary (POC and $CaCO_3$) and lithospheric (organic and inorganic) carbon storage. Note that the y-axis scale is an order of magnitude larger in b) than in a).

Introducing sediments (and a constant weathering flux) also changes carbon cycle dynamics over multiple glacial cycles. Fig S3 shows the transient changes in the simulated carbon reservoirs in simulation BASE over the entire simulated time period. In our set-up, carbon exchange between the atmosphere, ocean and sediments reacts to climatic and biogeochemical changes while weathering input fluxes of DIC, alkalinity and PO_4^{3-} are constant over time. A carbon flux imbalance arises during glacial phases in this open system. Under purely physical forcings, export fluxes from the photic zone decrease during glacial phases. Despite locally increased sedimentary POC preservation, global sediment accumulation rates decrease. In consequence, sequestration of $CaCO_3$ and POC from the reactive sediments (i.e. sediment burial) is reduced as well, since it is governed by the mass accumulation rate. The carbon which would have otherwise been buried instead accumulates as DIC in the ocean. Acceleration of sediment mass accumulation rates during glacial terminations increases sediment burial, which reduces marine DIC. The strength of these carbon cycle responses depends on the forcing strength, which varies between glacial cycles. The lukewarm interglacials of the first 350 kyr of our simulations do not restore the export fluxes and sedimentary $CaCO_3$ preservation required to re-balance the geologic carbon cycle, and so marine DIC concentrations are persistently higher during 800-450ka than at PI. Interglacials of the last 450kyr of the simulation reduce DIC in the long-term because they are warm and long enough for increased carbon transfer into sediments and sediment burial.

S4. Effects of additional forcings and Earth system changes on carbon fluxes

The previously described carbon cycle changes vary when further forcings and Earth system changes are applied.

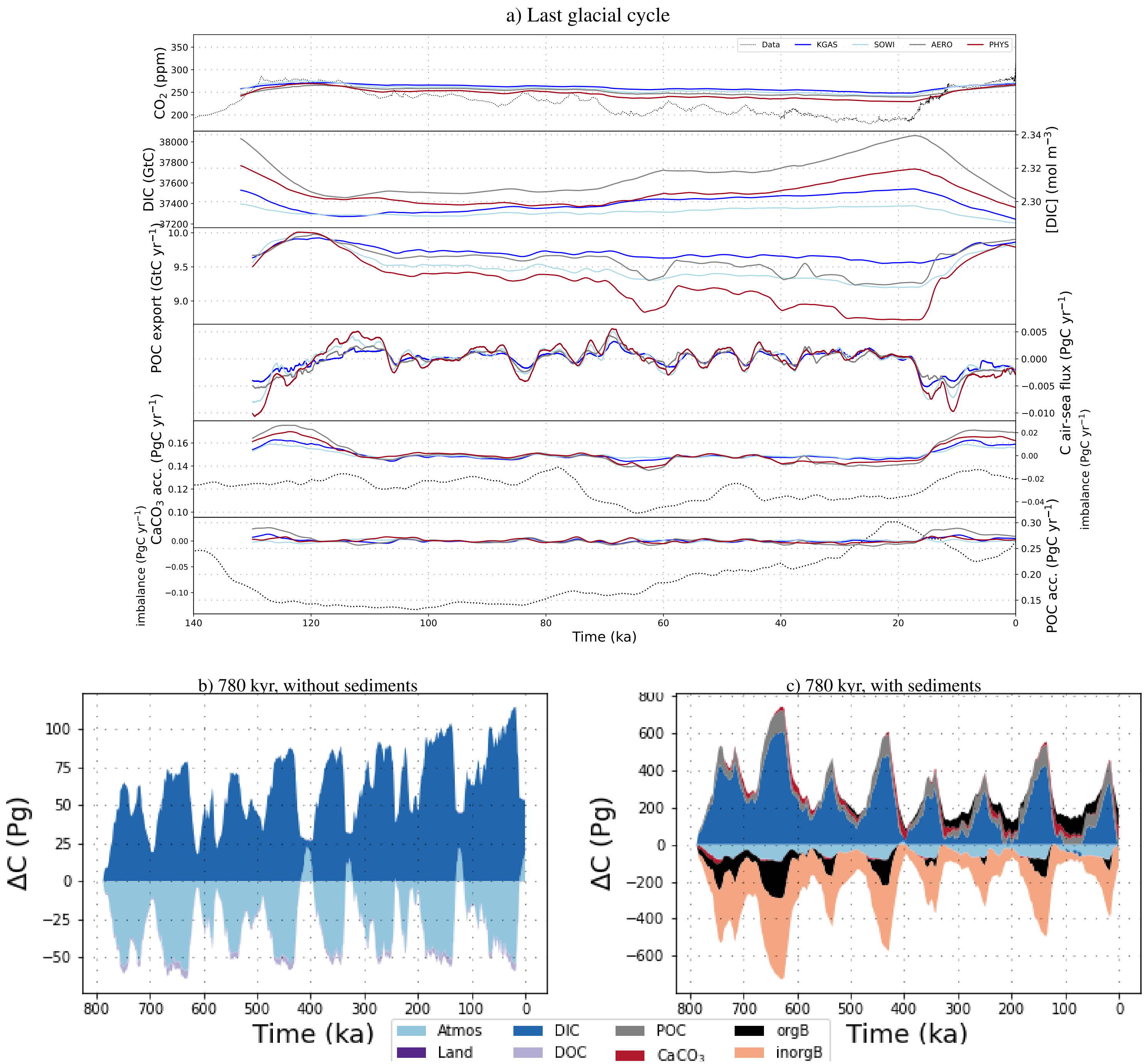

Figure S4. a) Atmospheric CO_2 concentrations, DIC and carbon fluxes over the most recent full glacial cyle in simulations with additional physical forcings in an open system. b) Transient carbon reservoir size changes across the last 780 kyr as simulated with all additional physical forcings combined in a closed system and c) in an open system. Shown are the size changes of atmospheric, terrestrial, marine (DIC and DOC), sedimentary (POC and $CaCO_3$) and lithospheric (organic and inorganic) carbon storage. Reservoir changes for individual forcings are displayed in Fig S24. Flux timeseries for simulations in a closed system are displayed in Fig S25.

Additional physical forcings result in roughly 1.5x larger carbon fluxes (Fig. S4), partially by amplifying the processes under the standard forcing and partially by introducing additional ones. Additional reduction of wind stress in the Southern Ocean (simulation SOWI) leads to a stronger isolation of deep Pacific water masses, reducing benthic oxygen levels. With dynamic sediments, more organic matter and $CaCO_3$ reaching the sediments is preserved due to the reduced oxygen concentrations, particularly in Pacific upwelling zones. This results in a larger net removal of nutrients and carbon from the ocean during glacial times which would have otherwise been released at intermediate depth. In consequence, wind stress forcing over the Southern Ocean reduces the carbon content of Pacific deep water when dynamic sediments are considered, despite an increase in water mass age. The re-ventilation of the deep Pacific during glacial termination leads to rising benthic oxygen concentrations. Due to the lower storage of dissolved nutrients and carbon in the glacial deep ocean, the potential to upwell nutrients during deglaciation is reduced, suppressing the spike in POC burial during terminations seen under the standard forcing and reducing PIC burial during these transition phases.

Reducing the transfer velocity of CO_2 in the Southern Ocean during glacials (simulation KGAS) also reduces CO_2 outgassing in the Southern Ocean which increases DIC in the deep Pacific but leaves ocean circulation unaffected, which reduces its global impact and, unlike the wind forcing, does not trap nutrients in the deep Pacific.

The AMOC slow-down in simulations with an additional reduction of incoming radiation during glacial phases and especially glacial maxima (e.g. via aerosol dimming, simulation AERO) creates an old, nutrient-rich and O_2-poor bottom water mass in the glacial Atlantic. Unlike with a vigorous AMOC, nutrients are not returned as quickly to the surface Atlantic but accumulate in the deep. The additional cooling combined with reduced nutrient supply reduces POC and $CaCO_3$ export in the Atlantic. In the North, where sea ice extent is increased and temperatures drop the most, they cease entirely. Globally, the additional cooling increases CO_2 and O_2 solubility. Overall these effects increase glacial carbon storage in the deep ocean. With dynamic sediments, the reduced $CaCO_3$ export in the North Atlantic raises the local lysocline, causing dissolution and increased marine DIC concentrations. The sudden shift in water masses when AMOC resumes during deglaciation amplifies the spike in burial rates observed under the standard forcing.

The different carbon and nutrient fluxes under these forcings change the total carbon and nutrient inventories in simulations with an open system, resulting in different DIC and nutrient concentrations at the start of the last glacial cycle and at the end of the runs.

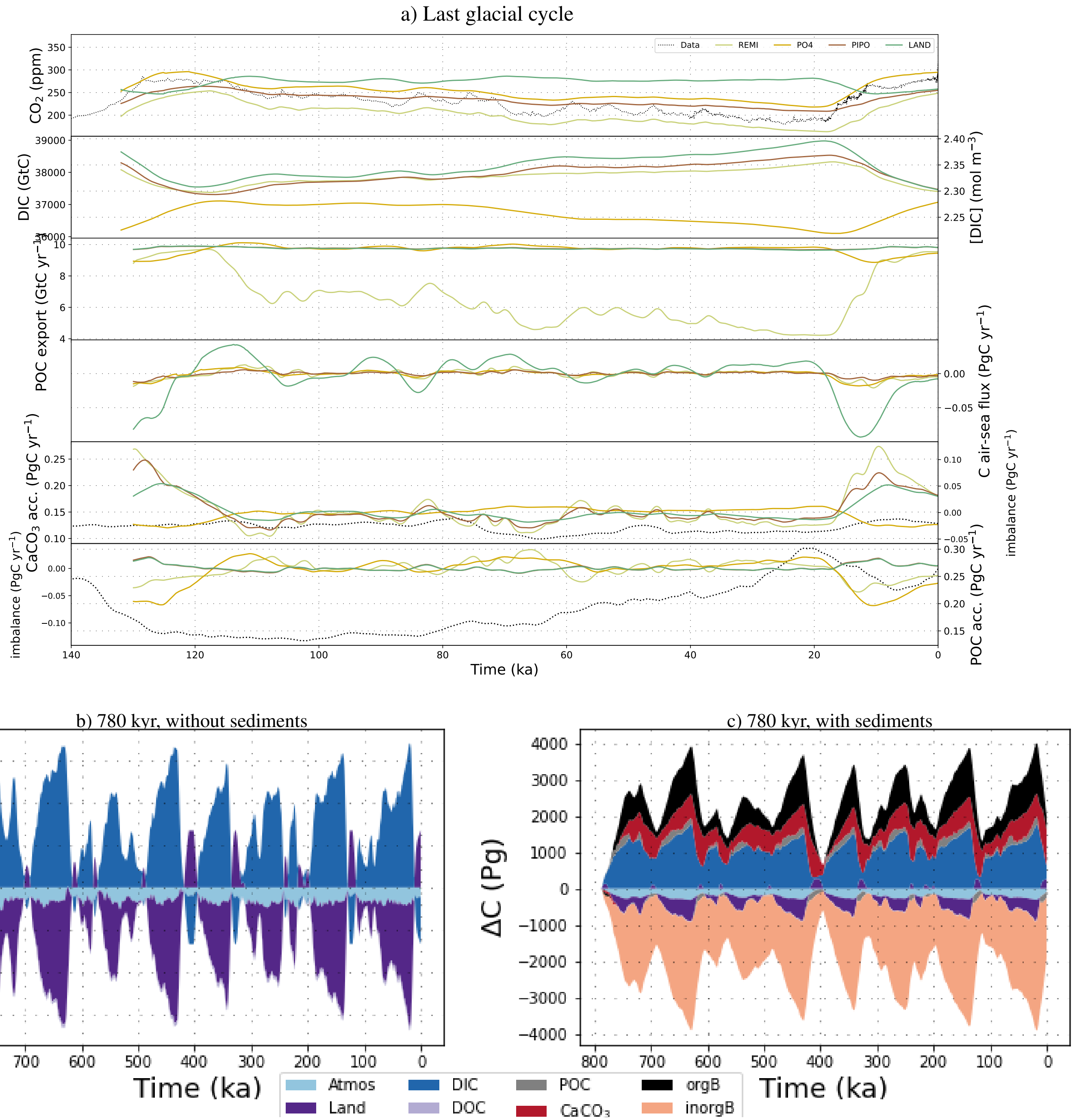

Figure S5. a) Atmospheric CO_2 concentrations, DIC and carbon fluxes over the most recent full glacial cyle in simulations with additional biogeochemical forcings in an open system. b) Transient carbon reservoir size changes across the last 780 kyr as simulated with all additional biogeochemical forcings combined in a closed system and c) in an open system. Shown are the size changes of atmospheric, terrestrial, marine (DIC and DOC), sedimentary (POC and $CaCO_3$) and lithospheric (organic and inorganic) carbon storage. Reservoir changes for individual forcings are displayed in Fig S26 and S27. Flux timeseries for simulations in a closed system are displayed in Fig S28.

Biogeochemical forcings affect carbon transfer primarily through the biological pump and the size of the terrestrial carbon sink. Nutrient inputs during glacial phases in simulation PO4 increase POC and $CaCO_3$ export, and sedimentary burial rates through increased sedimentary mass accumulation and lower O_2 concentrations in the deep ocean (Fig S5). During glacial termination, the prescribed nutrient supply to the surface ocean stops before the deep ocean is fully re-ventilated and the nutrients that accumulated in intermediate and deep water masses have returned to the surface. This delay results in low nutrient concentrations in the surface ocean, a transient drop in POC export, and consequentially burial fluxes. The reduced carbon burial raises DIC and increases the net carbon transfer from surface waters to the atmosphere during deglaciation. In consequence, when nutrients are added to a glacial ocean with responsive sediments, glacial phases become the dominant periods of organic and inorganic carbon sediment burial, reducing the accumulation of marine DIC and increasing the marine uptake of atmospheric CO_2 during glacial phases. This simulation PO4 yields the temporal CO_2 evolution which most closely resembles reconstructions from ice cores.

Reducing the PIC:POC ratio of export production during glacial phases (simulation PIPO) increases alkalinity in the surface ocean which enhances marine carbon uptake from the atmosphere, resulting in an additional CO_2 drawdown of up to $\sim$10ppm without sediments. This effect is enhanced by 20ppm when dynamic sediments are considered. When the export production is tilted towards organic matter production in an ocean with interactive sediments, reduced $CaCO_3$ export during inceptions and glacial periods translate into reduced $CaCO_3$ burial rates. This leads to a shoaling of the carbonate compensation depth, a build-up of alkalinity in the ocean and increased carbon transfer from the atmosphere to the ocean. The reduced sedimentary carbonate accumulation reduces the total mass flux to the sediments. On extratropical continental slopes, the reduced mass accumulation slows organic carbon burial, retaining more nutrients in the ocean and decreasing O_2 concentrations through continued remineralization instead. On continental slopes under upwelling areas with high productivity, the reduced O_2 expands the O_2 minimum zones, an effect which outweighs the local reduction of carbonate export and results in higher POC burial rates despite less carbonate deposition. Restoration of the interglacial PIC:POC ratio during deglaciation then enhances sedimentary carbonate deposition in benthic waters with higher pH and larger O_2 minimum zones than under the standard forcing, increasing the temporal spikes in carbonate and POC burial. Reduced glacial PIC:POC increases $CaCO_3$ burial events during glacial terminations.

Lowering the remineralization depth of organic matter in the glacial water column (simulation REMI) leads to a net carbon and nutrient transfer from the surface ocean to intermediate and deep water masses, where more O_2 is consumed. Without dynamic sediments, the increased DIC concentrations in the deep ocean increases the carbon storage of the glacial ocean. In addition, the reduced dissolution of POC in the upper water column during glacials increases surface ocean pH and CO_2 uptake by the ocean. With dynamic sediments, the resulting reduction in deep ocean O_2 concentration increases POC preservation in sediments below high productivity zones, e.g. tropical continental margins and upwelling areas. Where the larger flux of POC reaching the sediments is not preserved, it is remineralized, reducing the stability of sedimentary $CaCO_3$. Glacial inceptions are then characterized by increased POC and POP fluxes into the sediments and reduced $CaCO_3$ burial. During glacial terminations, POC is increasingly remineralized at shallower depth again, leading to reduced POC fluxes into the deep ocean and POC burial compared to the glacial phase. Surface ocean pH decreases and carbon is returned to the atmosphere. Compared to the standard forcing, lowering the remineralization depth thus shifts the timing of maximal POC burial rates from the interglacial to the glacial and amplifies the transient spike in $CaCO_3$ burial as increased nutrient supply during glacials does, but it also increases sedimentary $CaCO_3$ dissolution during glacial phases.

Land carbon release to the atmosphere during glacial phases (simulation LAND) invades and acidifies the ocean due to increased atmospheric concentrations, growing the marine DIC reservoir during glacials with and without dynamic sediments, resulting in the biggest glacial marine DIC reservoirs across our simulations. When interactive sediments are considered, this marine carbon uptake reduces $CaCO_3$ preservation and leads to a shoaling of the lysocline. During termination, as the external carbon addition subsides, the ocean vents carbon back into the atmosphere, transiently allowing for increased $CaCO_3$ burial.

The previous paragraphs show that varying biogenic particle production in the surface ocean is only a relevant control on marine carbon storage changes when interactive sediments are simulated. Instead, lowering the main remineralization depth (simulation REMI) and adding terrestrial carbon release during glaciation (simulation LAND) strongly influence marine carbon storage with and without dynamic sediments. Without dynamic sediments, they double the marine carbon uptake during glacial periods. When including interactive sediments, all biogeochemical forcings have substantially larger effects on the carbon cycle than physical changes, with 5-10x larger carbon fluxes than under the standard forcing (Fig S5).

S5. CO_2 restoring and non-linear effects of combined forcings on carbon fluxes

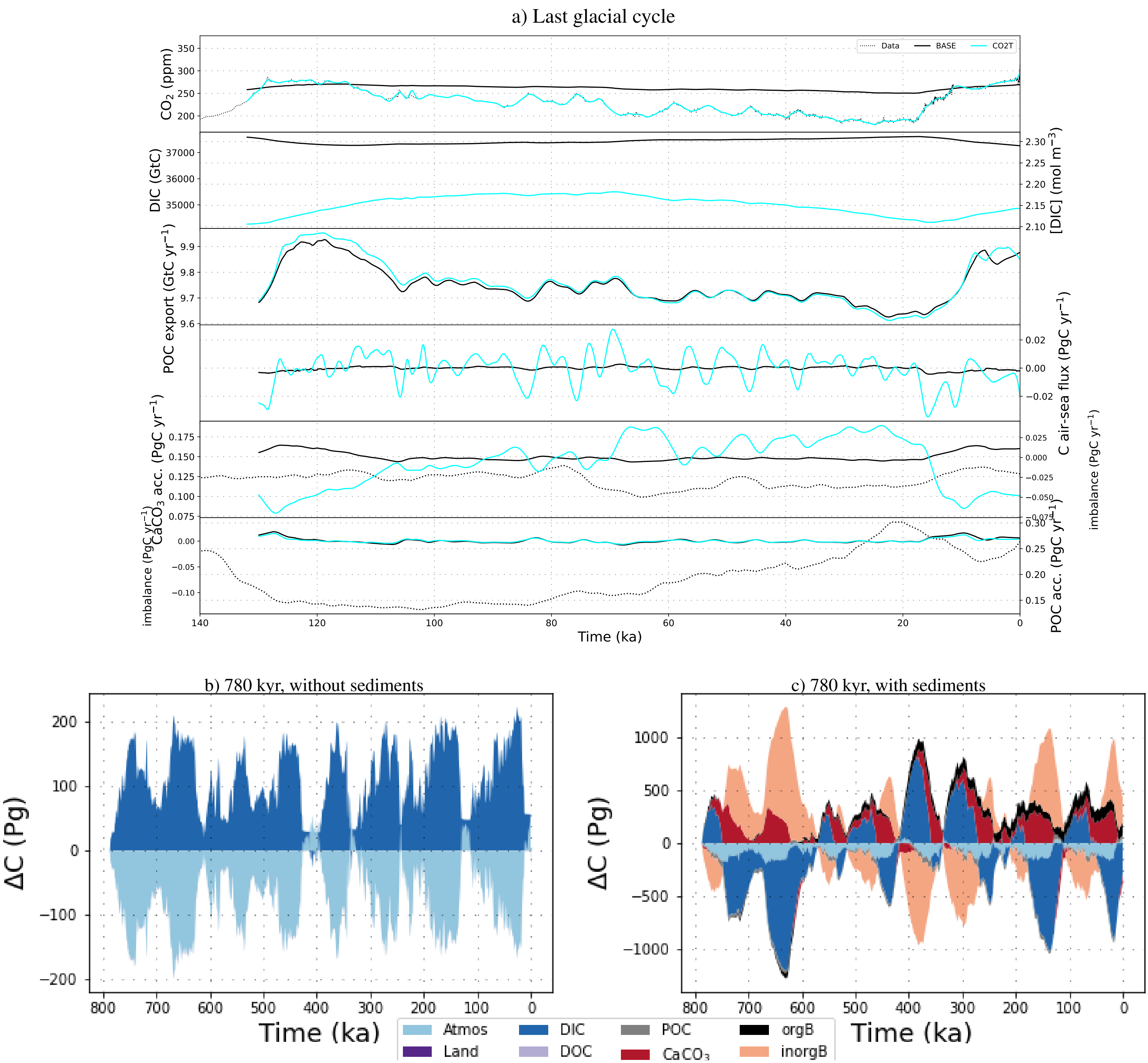

Figure S6. a) Atmospheric CO_2 concentrations, DIC and carbon fluxes over the most recent full glacial cyle in simulations BASE and CO2T in an open system. b) Transient carbon reservoir size changes across the last 780 kyr as simulated with alkalinity nudging in a closed system and c) in an open system. Shown are the size changes of atmospheric, terrestrial, marine (DIC and DOC), sedimentary (POC and $CaCO_3$) and lithospheric (organic and inorganic) carbon storage.

By design, the applied alkalinity nudging causes marine carbon uptake and release that shape atmospheric CO_2 in line with observations (Fig S6). As a consequence, the surface ocean is more alkaline in glacial times and more acidic during terminations than in the standard forcing, enabling increased marine carbon uptake. In simulations with dynamic sediments, $CaCO_3$ burial during cold phases is increased but the burial spike during terminations suppressed.

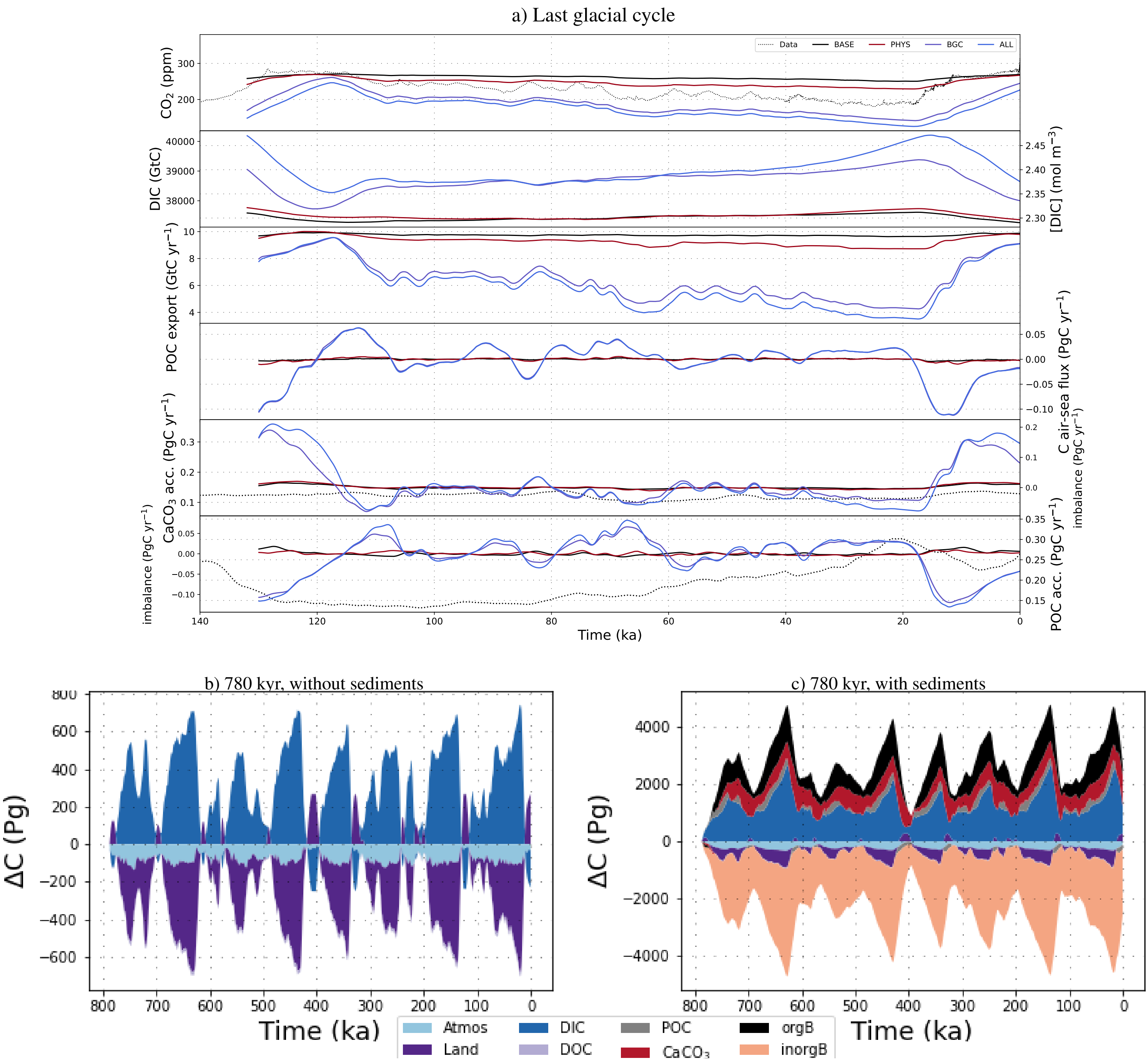

Figure S7. a) Atmospheric CO_2 concentrations, DIC and carbon fluxes over the most recent full glacial cyle in simulations with different combinations of additional forcings in an open system. b) Transient carbon reservoir size changes across the last 780 kyr as simulated with all additional forcings combined in a closed system and c) in an open system. Shown are the size changes of atmospheric, terrestrial, marine (DIC and DOC), sedimentary (POC and $CaCO_3$) and lithospheric (organic and inorganic) carbon storage. Flux timeseries for simulations in a closed system are displayed in Fig S29.

The three tested physical forcings combine almost linearly in their effect on atmospheric CO_2. Circulation change is dominated by radiation reductions, with strong AMOC weakening during glacials and some reduction of the PMOC, but less than in simulation SOWI because of increased sea ice cover in the Southern Ocean which limits the effect of wind stress changes. In consequence, the glacial deep ocean holds more nutrients when all forcings are combined: it has a large Atlantic reservoir due to sluggish overturning and a larger Pacific reservoir than in SOWI due to less organic carbon burial. During deglaciation, the release of these nutrients back into the surface ocean creates a larger productivity spike than when the forcings are applied individually, reducing marine $[O_2]$ further but causing only a minimal temporary reduction of <5 ppm in atmospheric CO_2 (Fig. S7). In simulations with interactive sediments, additional radiative forcing (AERO) and Southern Ocean wind forcing (SOWI) shift sedimentary $CaCO_3$ and POC accumulation rates in opposite directions. Yet, their effects on nutrient, temperature and oxygen distributions are almost additive.

While physical effects on carbon concentrations combine almost linearly, the combination of biogeochemical forcings is non-linear because they directly alter production and dissolution patterns in opposing ways. Acidification of benthic water masses through external nutrient (PO4) and carbon (LAND) supply during glacials counteracts the benthic pH increase under a deepened remineralisation depth (REMI). When all biogeochemical forcings are combined, net $CaCO_3$ fluxes into marine sediments are reduced during glacial maxima and increased during terminations, but the burial peak is delayed. Biogeochemical forcings dominate the carbon cycle response when all forcings are combined, except for the North Atlantic where circulation changes cause the biggest perturbation. The magnitude of the non-linearities that occur when all forcings are combined is similar to the combined effect of only the physical forcings.

Additional Figures

Table S1. Prescribed constant solute input into the surface ocean to balance steady-state interglacial sedimentary burial fluxes.

	DIC (GtC/yr)	ALK (Tmol eq/yr)	PO_4^{3-} (Tmol P/yr)	SiO (Tmol Si/yr)	$DI^{13}C$ (GtC/yr/$^{13}C_{std}$)
BASE	0.414	21.61	0.19	4.52	0.409

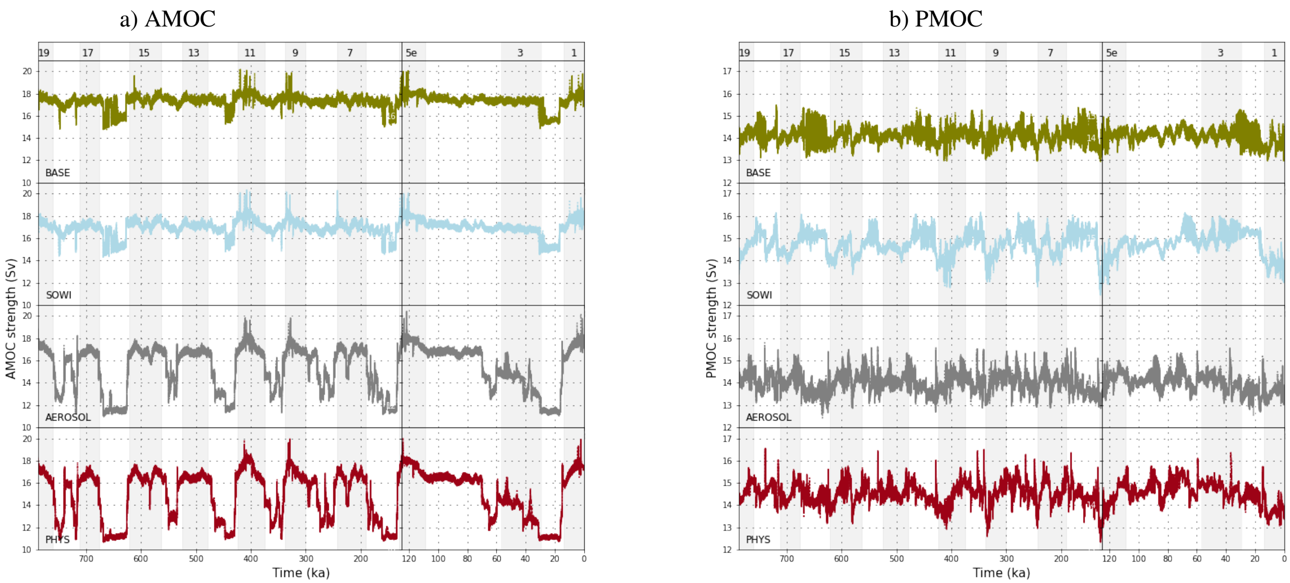

Figure S8. Transient variations of AMOC and PMOC strengths in simulations with different physcial forcings.

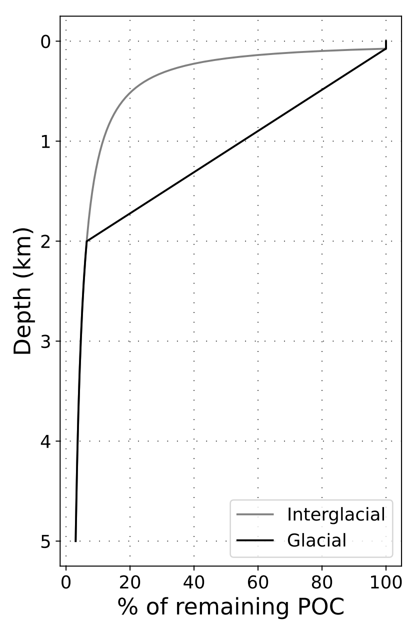

Figure S9. Comparison of the interglacial and glacial end-members of the prescribed remineralization profiles.

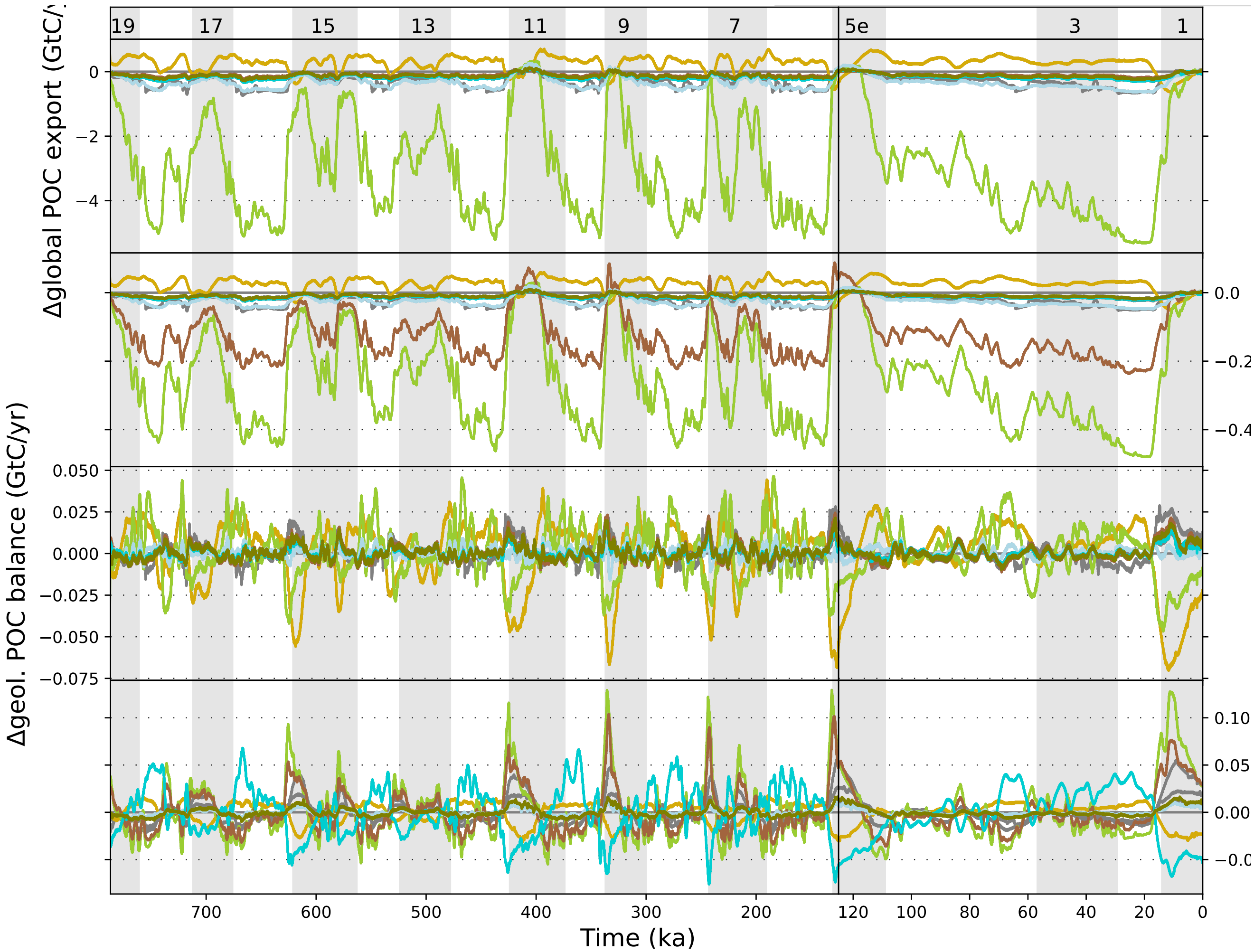

Figure S10. Transient variations of POC and $CaCO_3$ export production and geologic imbalance (i.e. the difference between accumulation of these materials in marine sediments and the constant supply into the surface ocean that mimics terrestrial weathering in our simulations) due to the applied forcings. Shown are the absolute results for each simulation. The results that are explicitly mentioned in the text are shown in colour, the others are shown in gray. Gray shading indicates uneven MIS as indicated at the top of the figure.

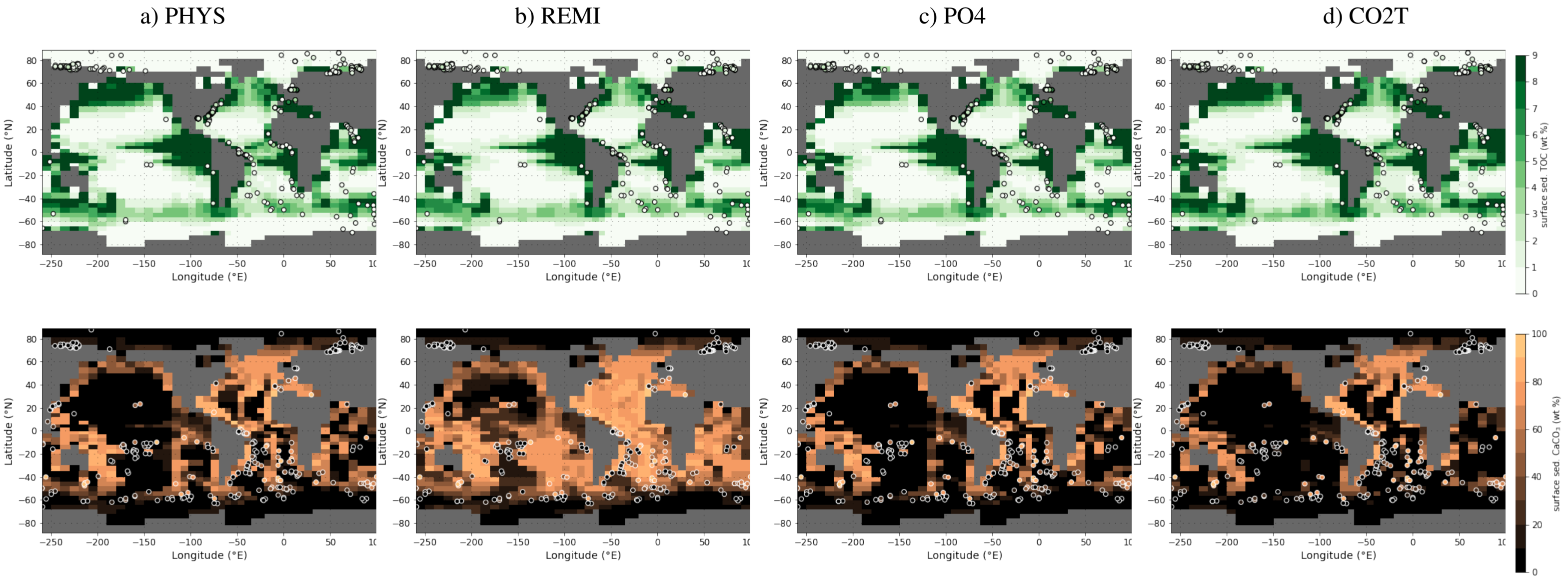

Figure S11. Sedimentary POC and $CaCO_3$ fractions during the late Holocene (Hayes et al., 2021) as reconstructed (circles) and in simulations PHYS, REMI, PO4 and CO2T (underlying maps). Shown are only data points that fall into the local benthic grid box of the model. The root mean square errors of simulated and reconstructed values are (from left to right): 7.6 %, 7.0 %, 7.6 % and 8.2 % for POC (top row) and 27.5 %, 25.7 %, 29.4 % and 31.4 % for $CaCO_3$ (bottom row).

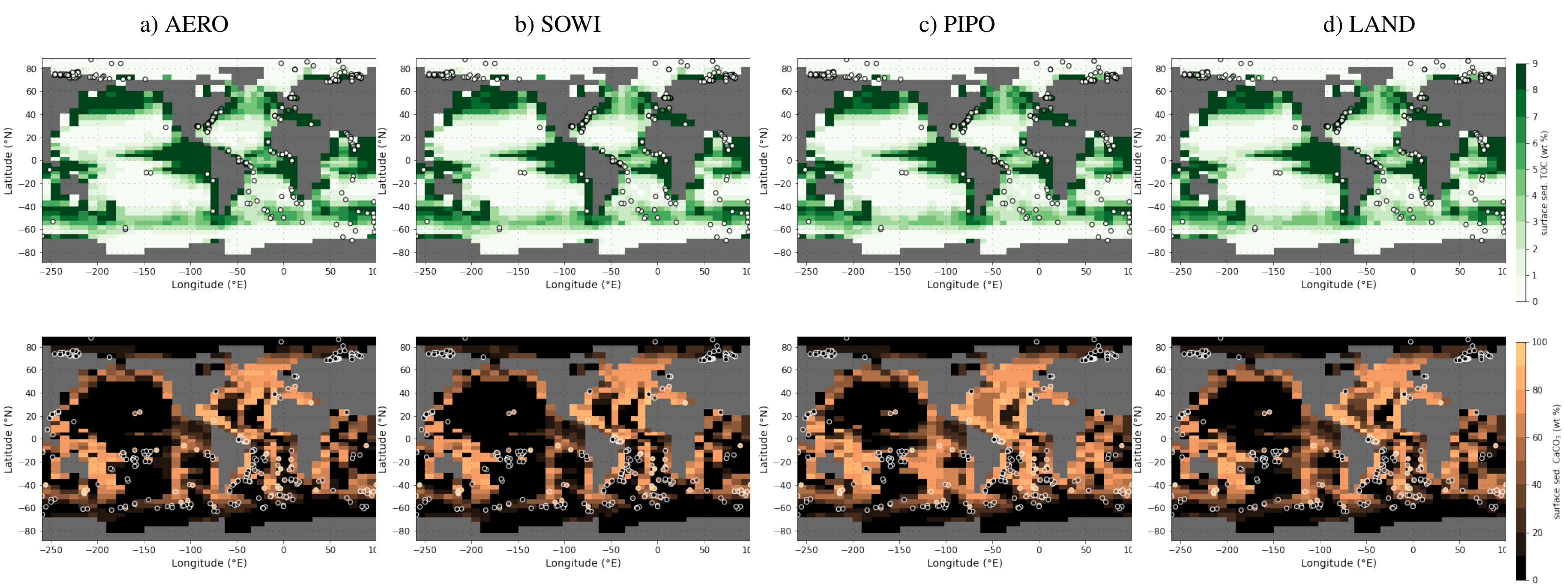

Figure S12. Sedimentary POC and $CaCO_3$ fractions during the late Holocene (Hayes et al., 2021) as reconstructed (circles) and in simulations AERO, SOWI, CACO and LAND (underlying maps). Shown are only data points that fall into the local benthic grid box of the model. The root mean square errors of simulated and reconstructed values are (from left to right): 8.8 %, 9.4 %, 7.6 % and 7.6 % for POC (top row) and 27.2 %, 27.8 %, 26.2 % and 26.6 % for $CaCO_3$ (bottom row).

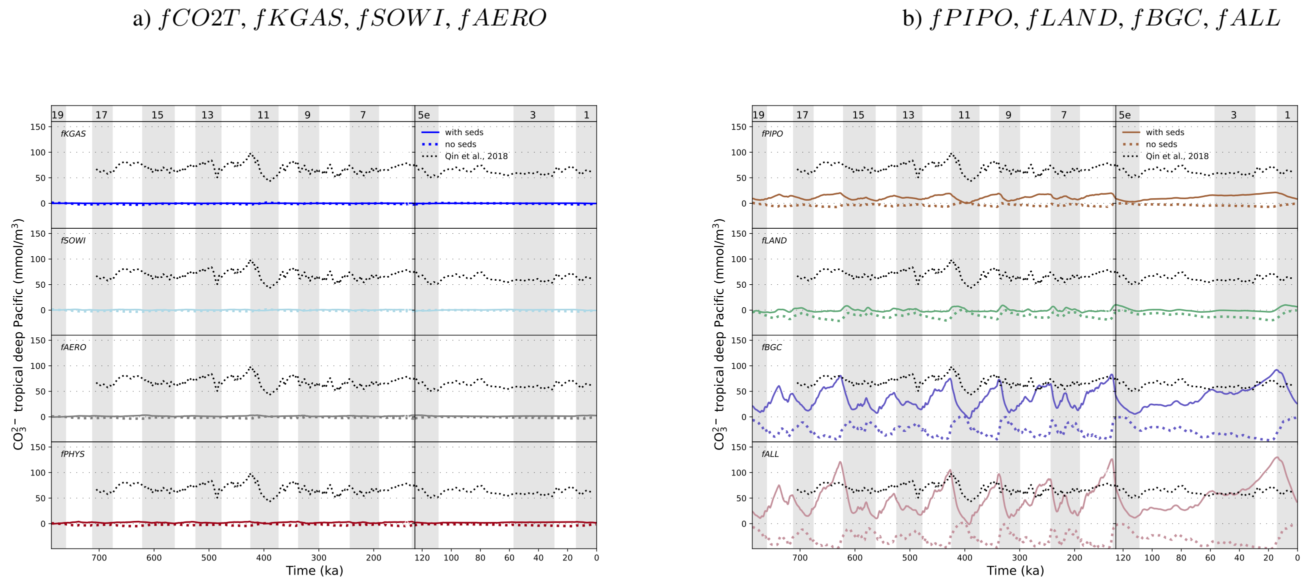

Figure S13. Transient variations of CO_3^{2-} in the tropical deep Pacific as simulated and reconstructed by Qin et al. (2018).

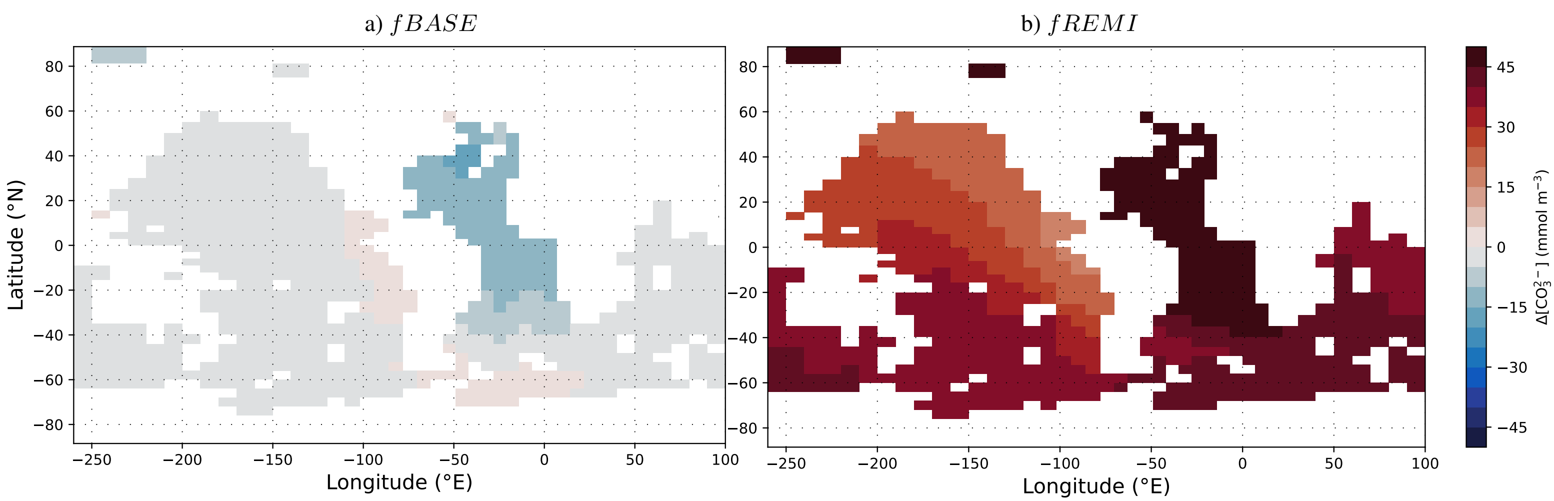

Figure S14. Selected factorial effects on simulated LGM-PI differences in deep CO_3^{2-} (3500 m depth).

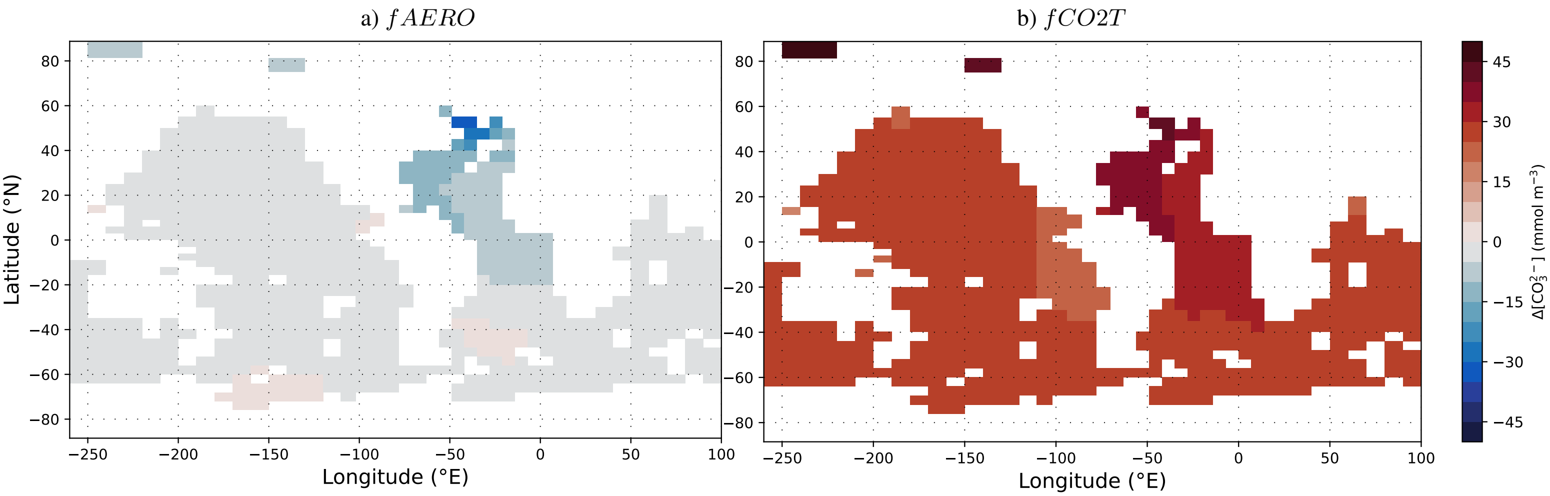

Figure S15. Selected factorial effects on simulated LGM-PI differences in deep CO_3^{2-} (3500 m depth).

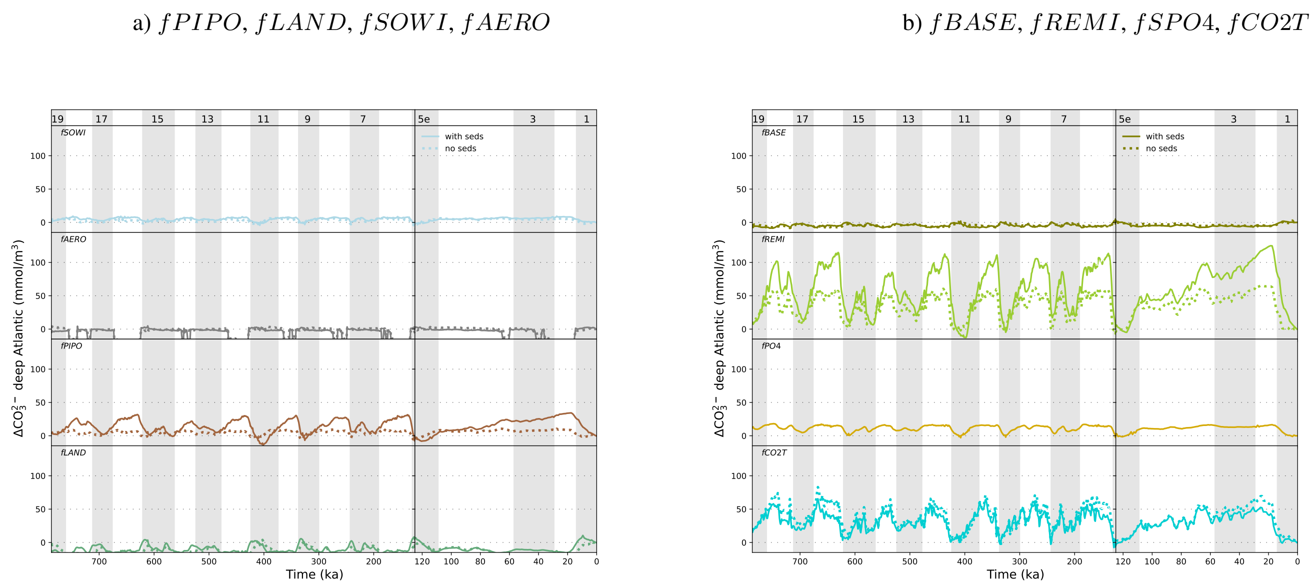

Figure S16. Transient variations of CO_3^{2-} in the deep North Atlantic (40-60 ◦N) as simulated in selected simulations.

a) BASE, KGAS, SOWI, AERO

b) PIPO, BGC, ALL, CO2T

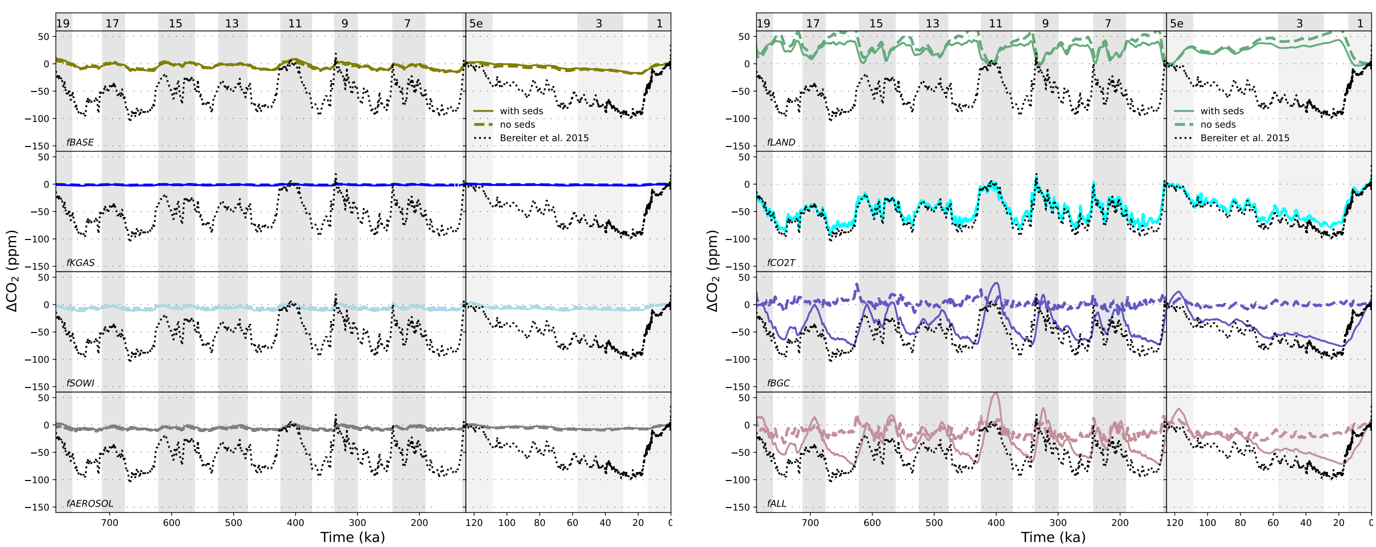

Figure S17. Transient variations of atmospheric CO_2 concentrations as simulated in the simulations not shown in Fig. 5 in the main text, and as reconstructed by Bereiter et al. (2015). Shown is the deviation from the respective pre-industrial value.

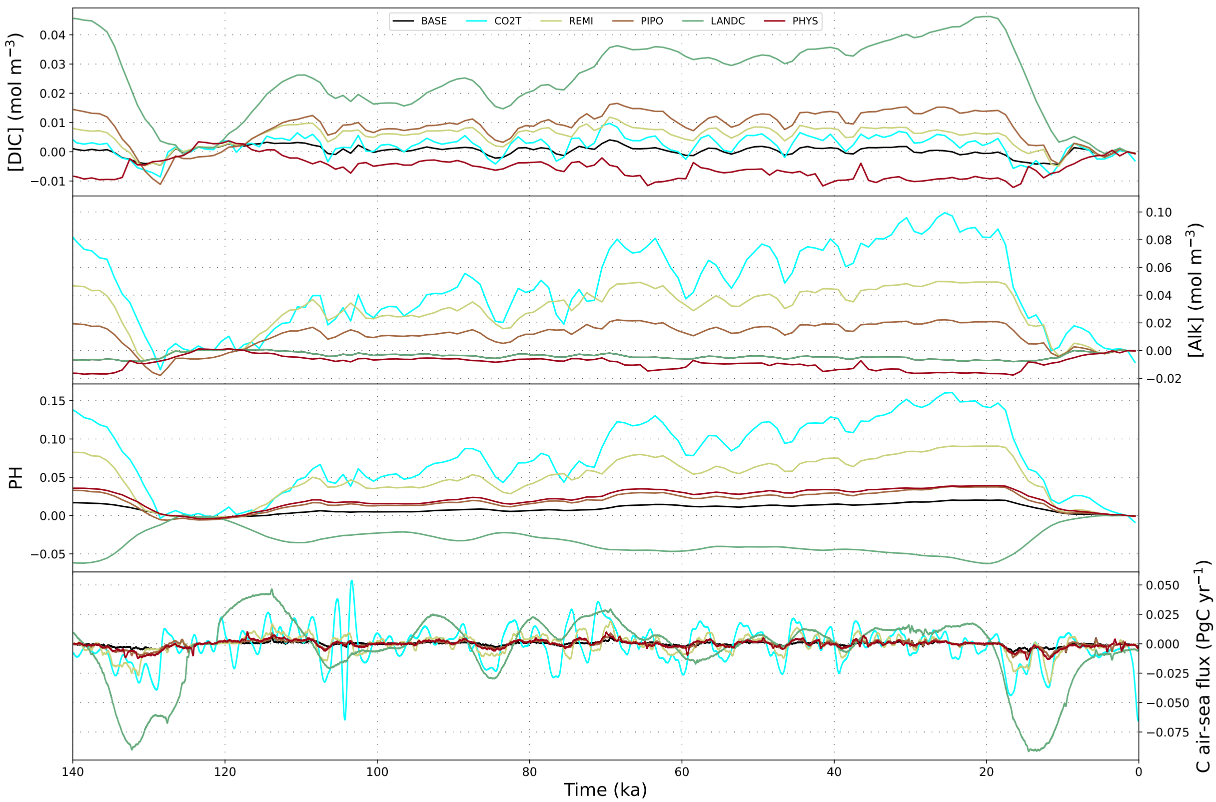

Figure S18. Globally-averaged changes in surface ocean carbonate system parameters in selected simulations without interactive sediments.

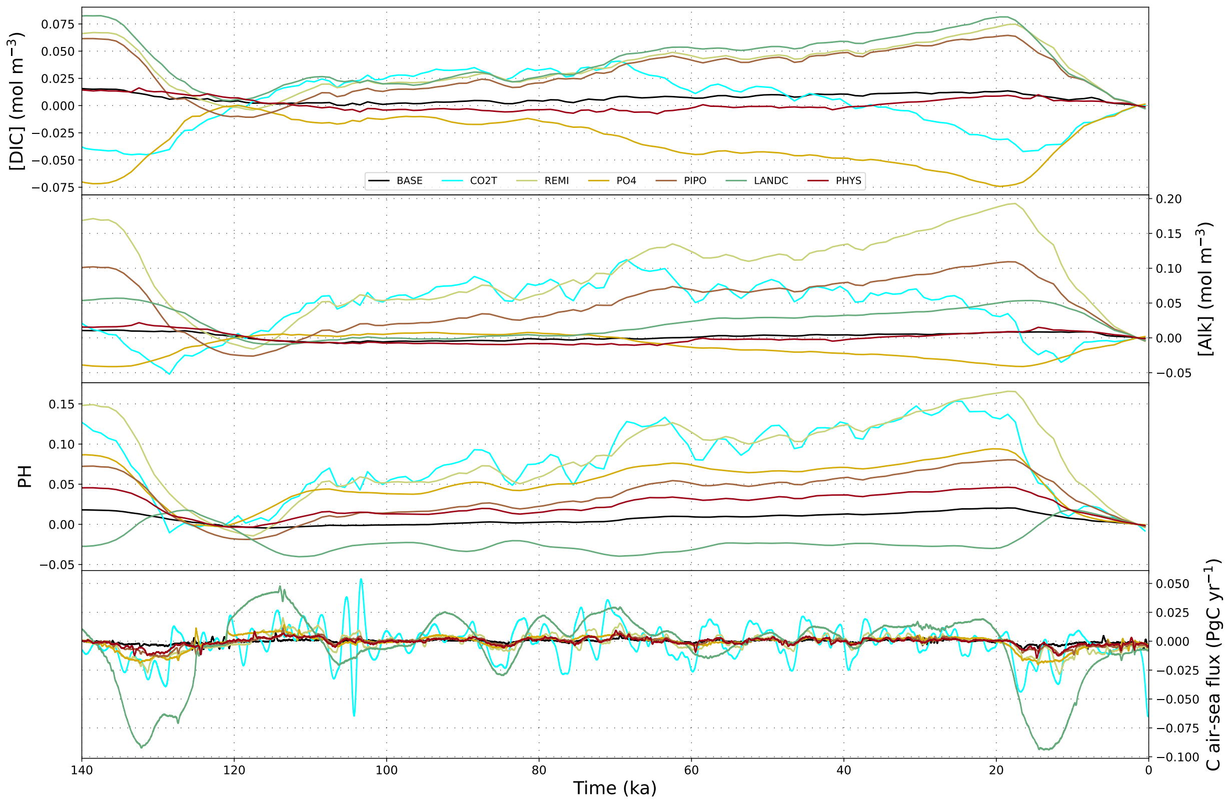

Figure S19. Globally-averaged changes in surface ocean carbonate system parameters in selected simulations with interactive sediments.

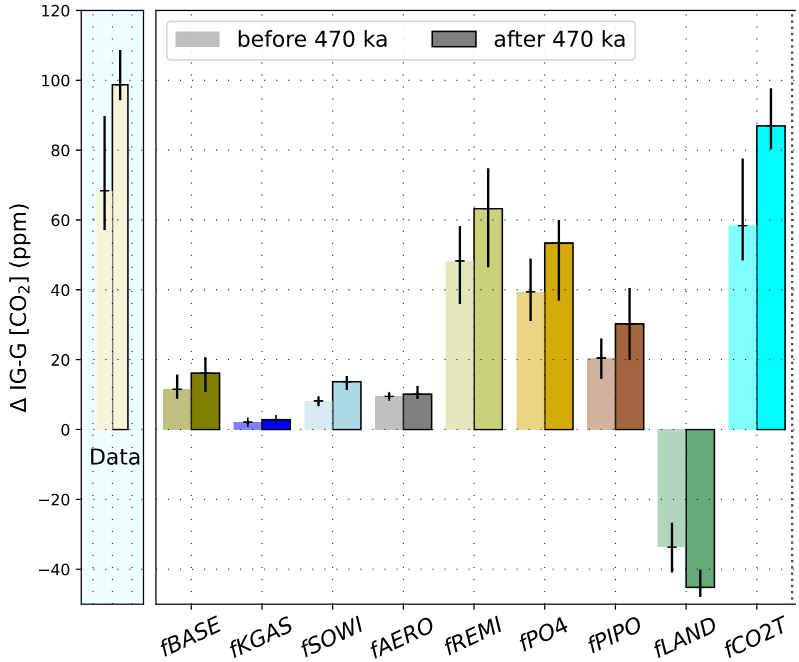

Figure S20. Difference of the glacial-interglacial atmospheric CO_2 amplitude before and after the MBT in our simulations compared to that in the reconstructed CO_2 record (Bereiter et al., 2015). For the results of the simulations without interactive sediments see Fig. S20

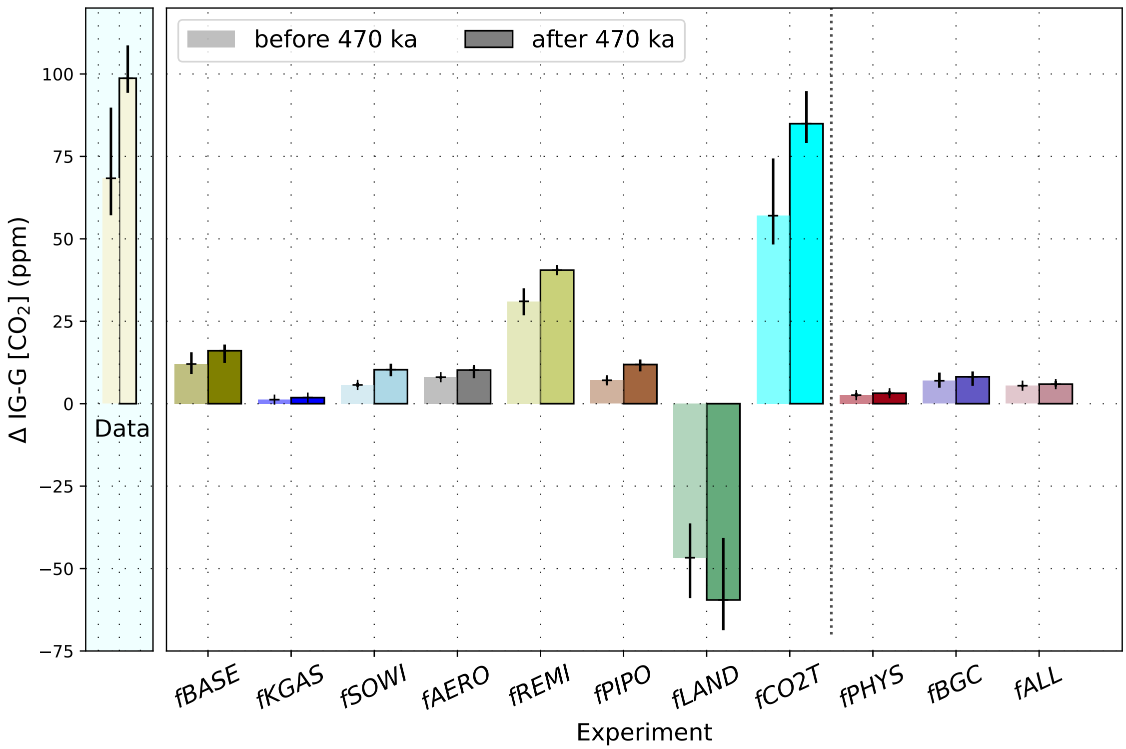

Figure S21. Difference of the glacial-interglacial atmospheric CO_2 amplitude before and after the MBT in our simulations without interactive sediments compared to that in the reconstructed CO_2 record (Bereiter et al., 2015, , horizontal black line).

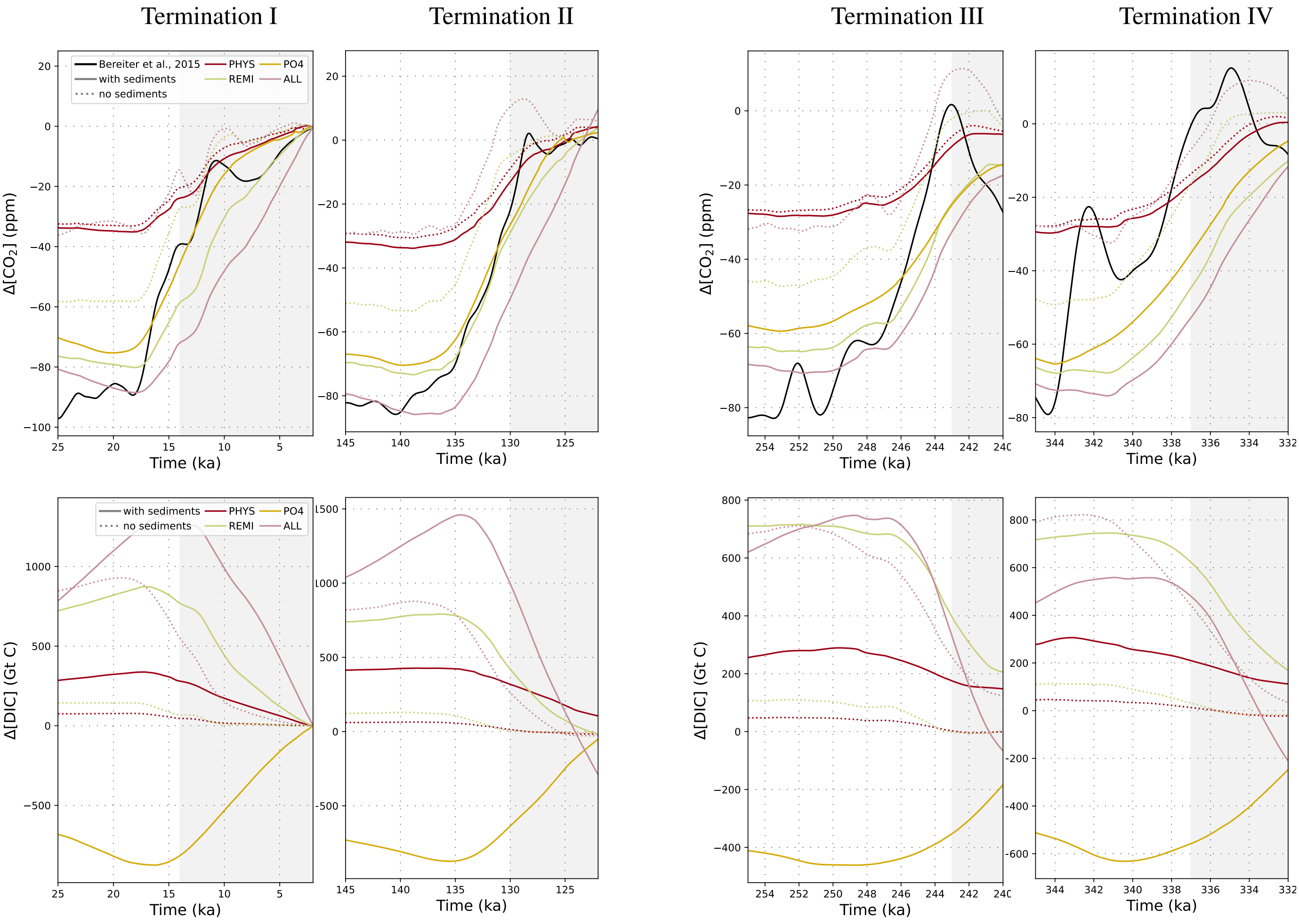

Figure S22. Reconstructed and simulated atmospheric CO_2 changes (upper row) and simulated DIC changes (lower row) across the last four deglaciations.

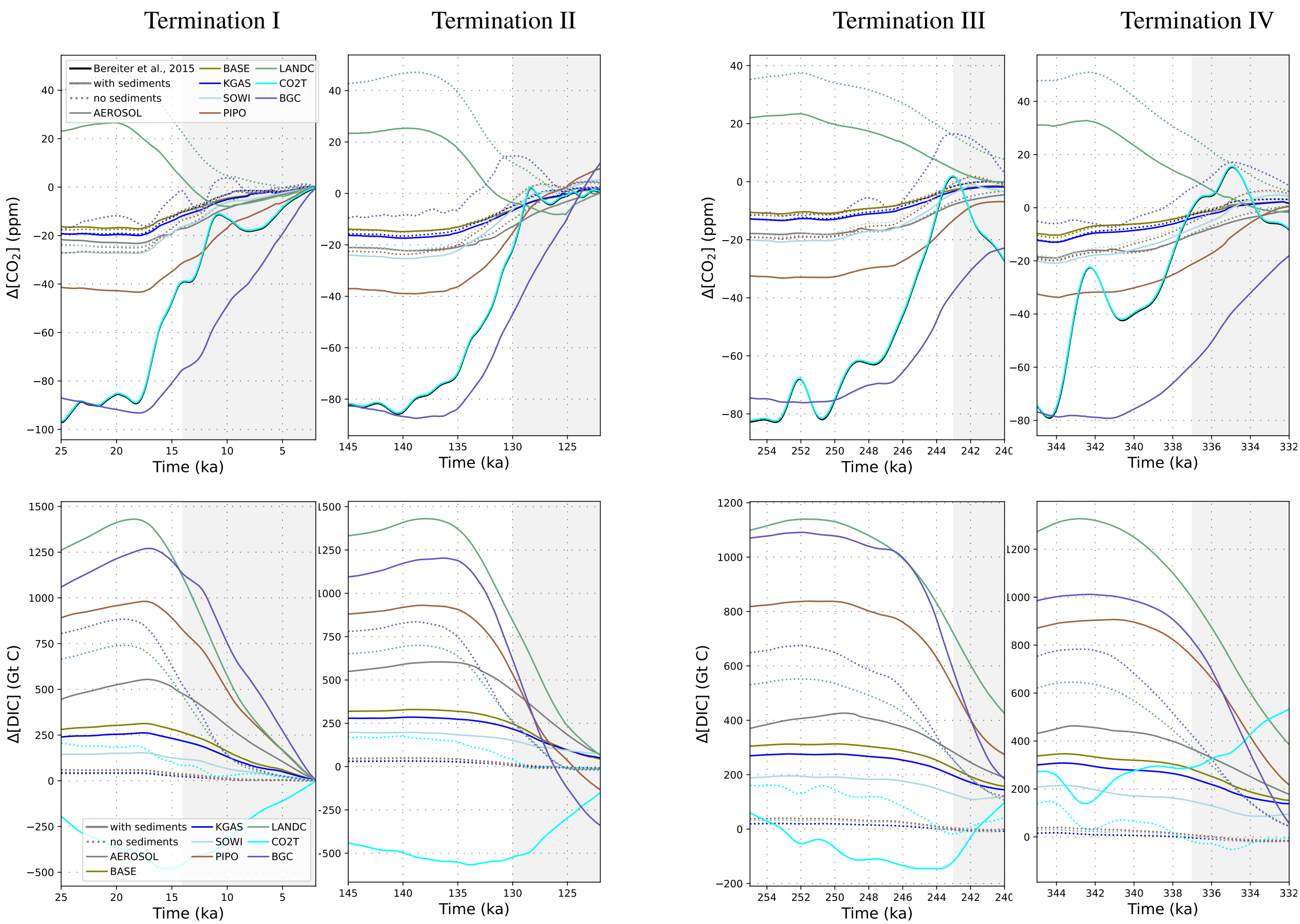

Figure S23. Reconstructed and simulated atmospheric CO_2 changes (upper row) and simulated DIC changes (lower row) across the last four deglaciations.

Table S2. Dynamical geologic carbon cycle imbalances (marine outputs - inputs) at the end of each simulation.

Simulation	DIC (GtC/yr)	ALK (Tmol eq/yr)	PO_4^{3-} (Tmol P/yr)	SiO (Tmol Si/yr)	$DI^{13}C$ (GtC/yr/$^{13}C_{std}$)
BASE	0.017	1.51	0.006	-0.06	0.017
KGAS	0.015	1.32	0.005	-0.06	0.014
SOWI	0.009	0.94	0.003	0.21	0.009
AERO	0.030	2.99	0.008	0.39	0.030
REMI	0.018	4.85	0.006	0.47	0.018
PHOS	-0.045	-3.47	-0.016	-0.13	-0.045
CACO	0.035	4.84	0.005	-0.04	0.035
LAND	0.035	4.66	0.005	-0.04	0.035
CO2T	-0.05	-8.86	0.005	-0.08	-0.05
PHYS	0.016	2.00	0.003	0.28	0.016
BGC	0.028	11.30	-0.026	0.53	0.028
ALL	0.096	22.69	-0.026	1.37	0.097

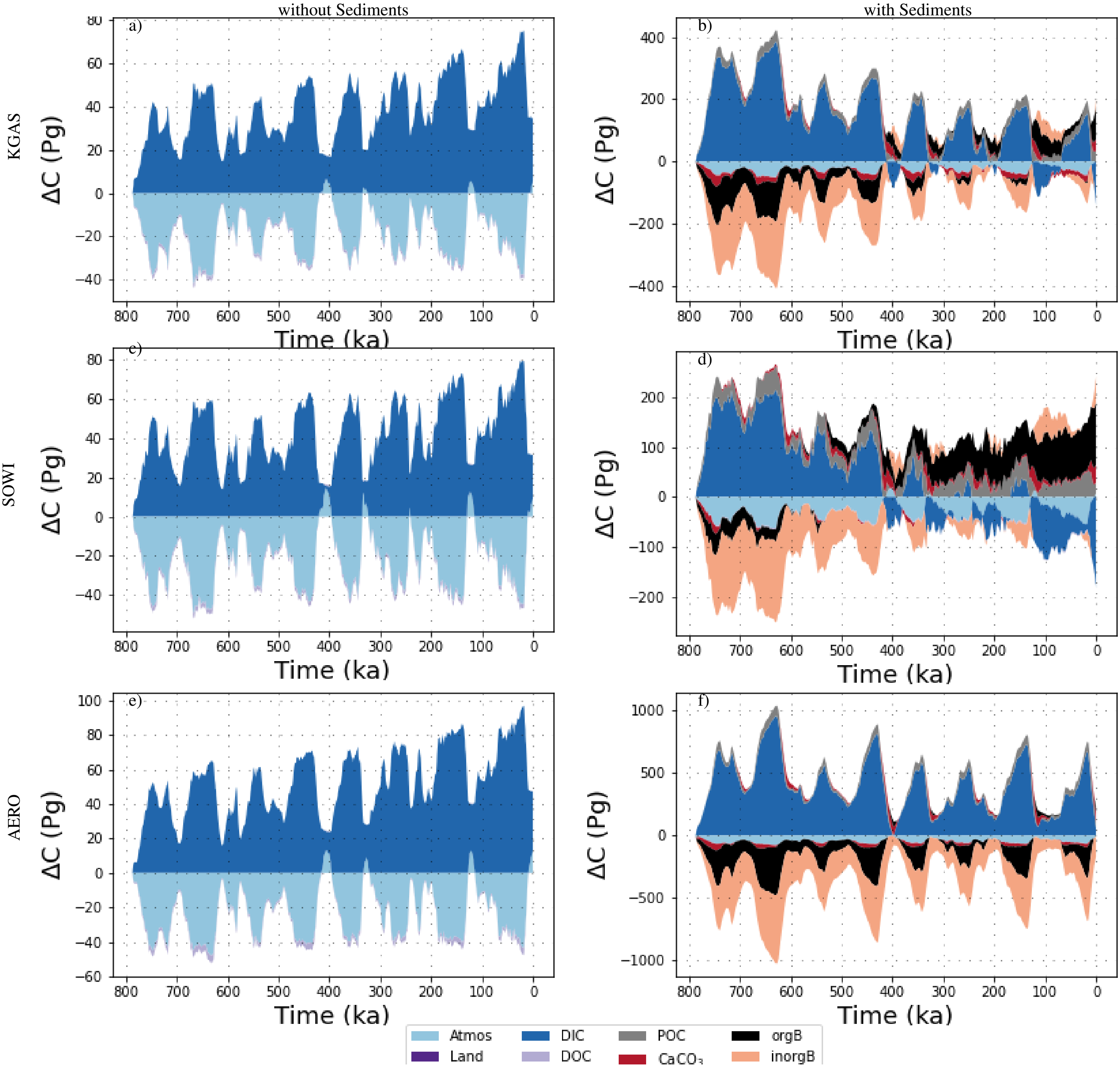

Figure S24. Transient carbon reservoir size changes across the last 780 kyr as simulated in simulations with the standard forcings plus additional physical forcings, left in a closed and right in an open system. Shown are the size changes of atmospheric, terrestrial, marine (DIC and DOC), sedimentary (POC and $CaCO_3$) and lithospheric (organic and inorganic) carbon storage.

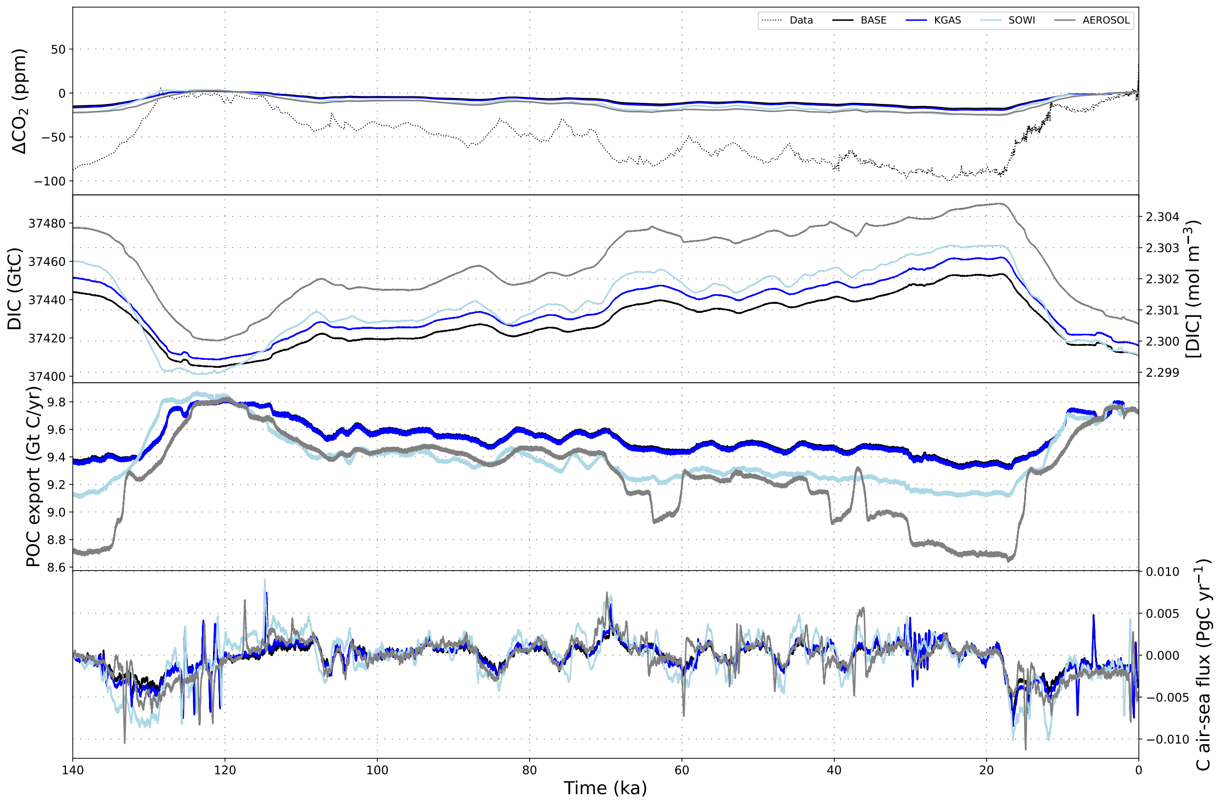

Figure S25. Atmospheric CO_2 concentrations, DIC and carbon fluxes over the most recent full glacial cyle in simulations with additional physical forcings and without dynamic sediments.

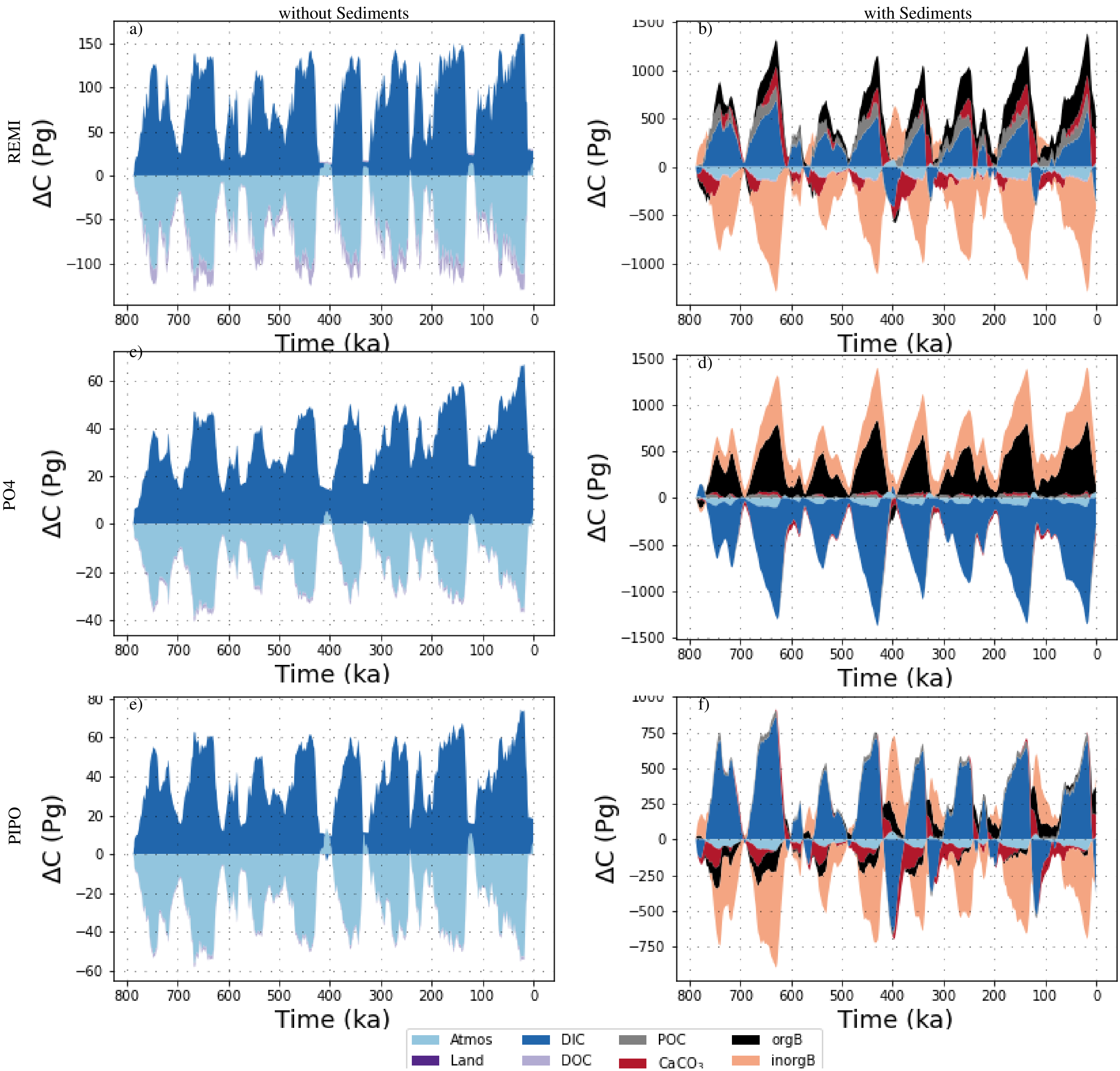

Figure S26. Transient carbon reservoir size changes across the last 780 kyr as simulated in simulations with the standard forcings plus additional biogeochemical forcings, left in a closed and right in an open system. Shown are the size changes of atmospheric, terrestrial, marine (DIC and DOC), sedimentary (POC and $CaCO_3$) and lithospheric (organic and inorganic) carbon storage.

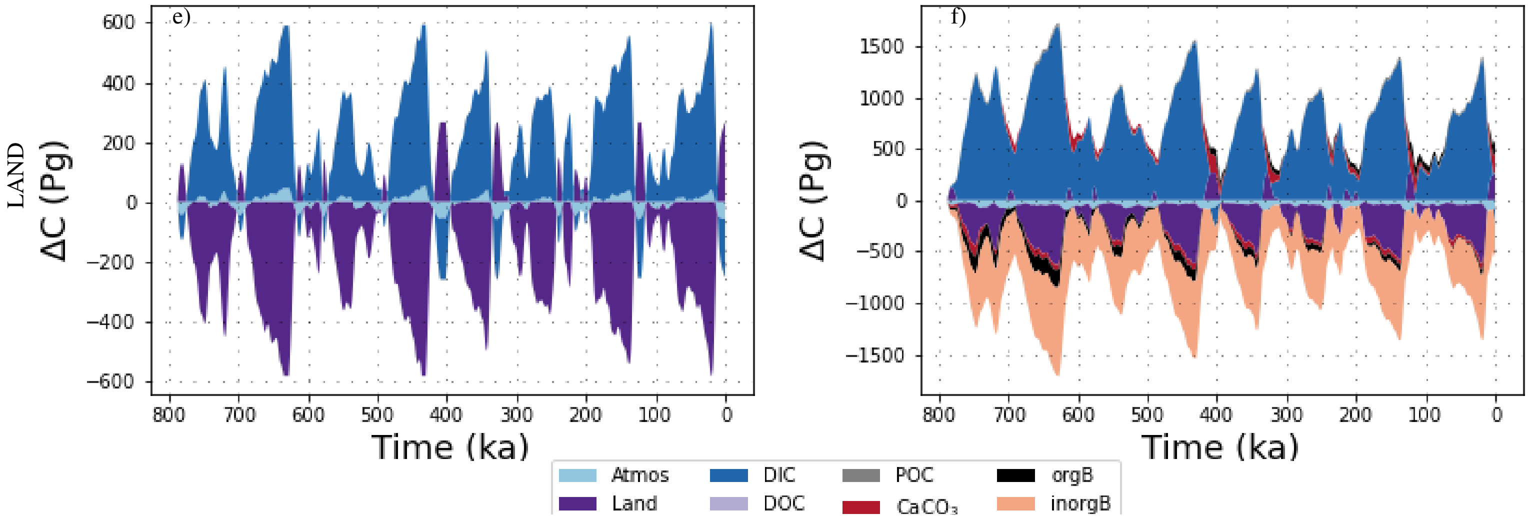

Figure S27. Transient carbon reservoir size changes across the last 780 kyr as simulated in simulations with the standard forcings plus terrestrial carbon fluxes, left in a closed and right in an open system. Shown are the size changes of atmospheric, terrestrial, marine (DIC and DOC), sedimentary (POC and $CaCO_3$) and lithospheric (organic and inorganic) carbon storage.

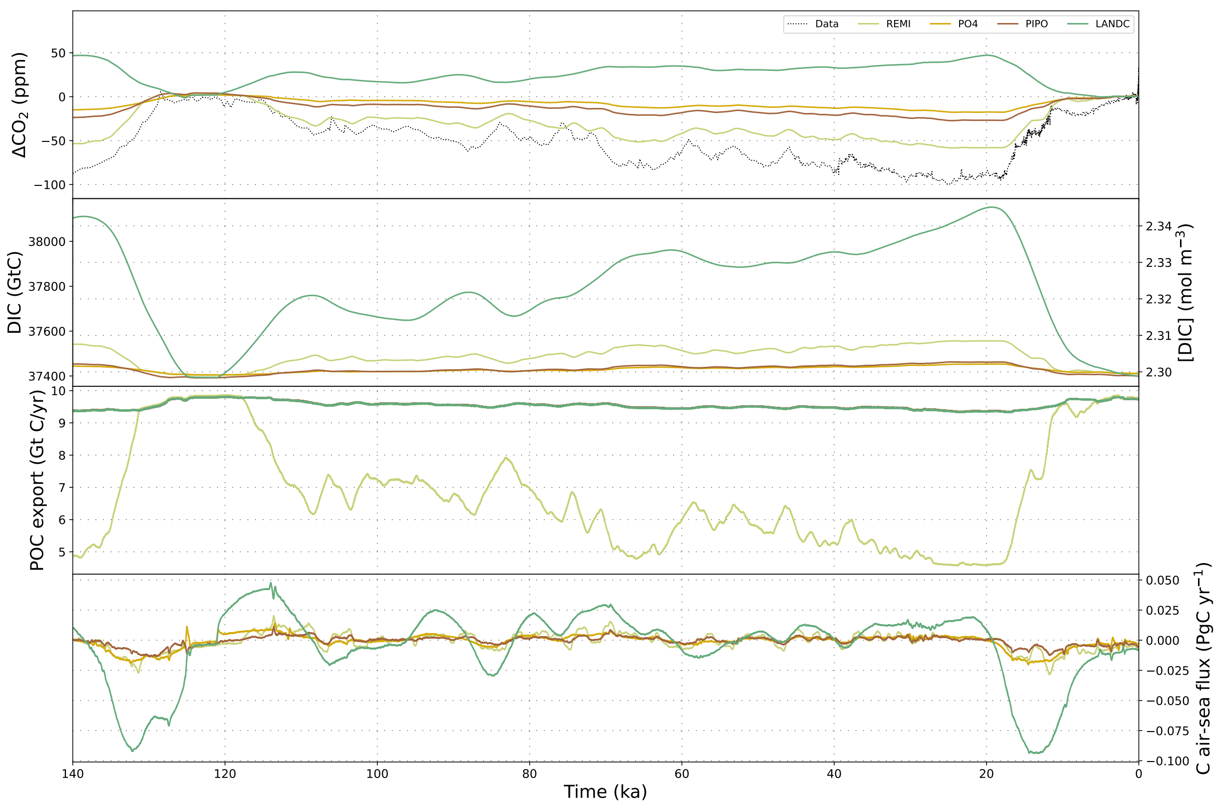

Figure S28. Atmospheric CO_2 concentrations, DIC and carbon fluxes over the most recent full glacial cyle in simulations with additional biogeochemical forcings and without dynamic sediments.

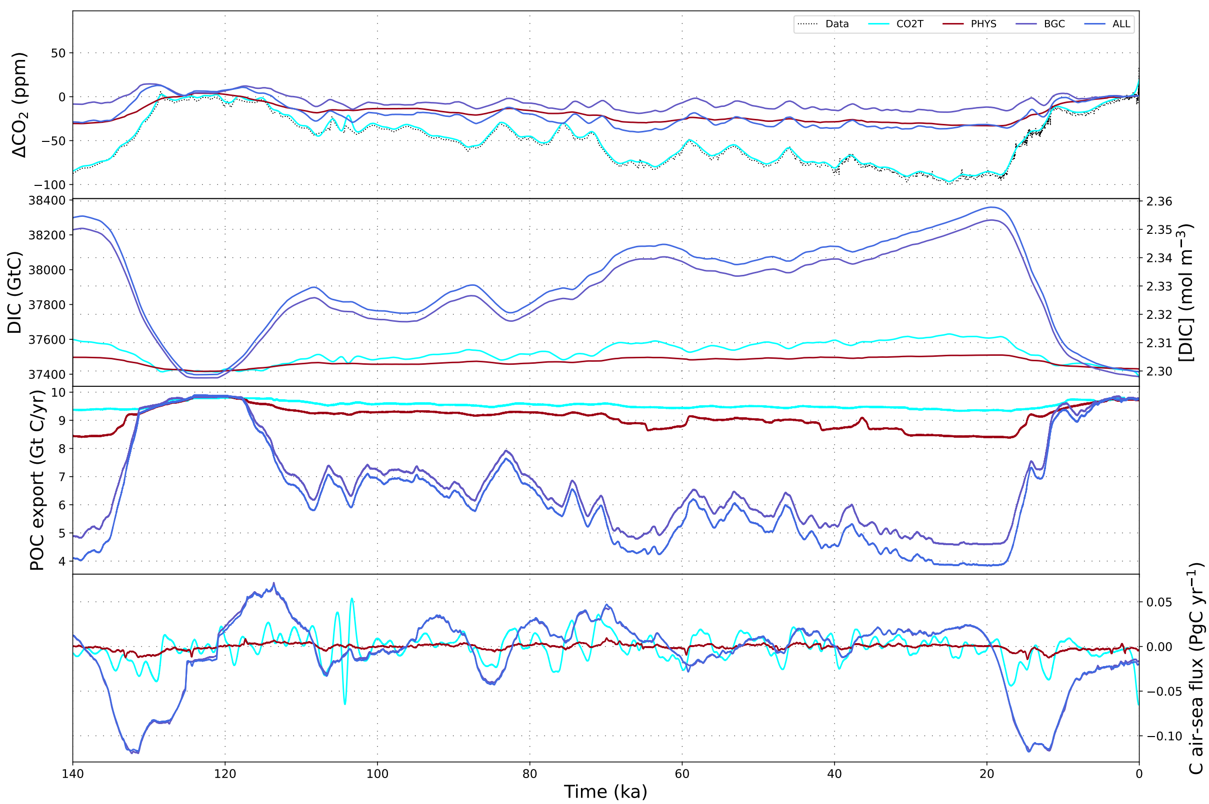

Figure S29. Atmospheric CO_2 concentrations, DIC and carbon fluxes over the most recent full glacial cyle in simulations with combinations of additional forcings and without dynamic sediments.

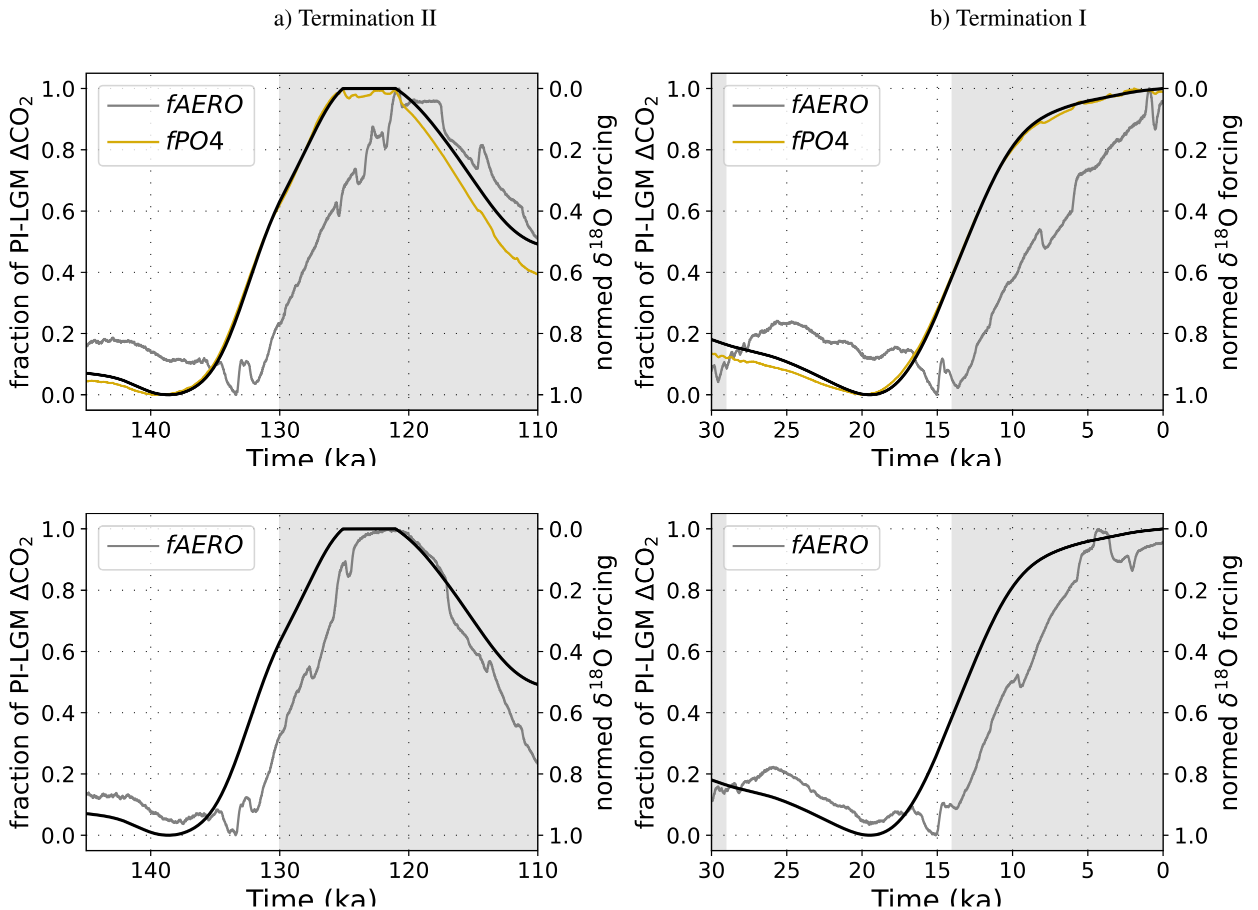

Figure S30. δ^{18}O-derived scaling of the prescribed forcing and the resulting simulated atmospheric CO_2, normalized by the respective PI-LGM CO_2 difference, in selected simulations with interactive sediments (top row) and without interactive sediments (bottom row).

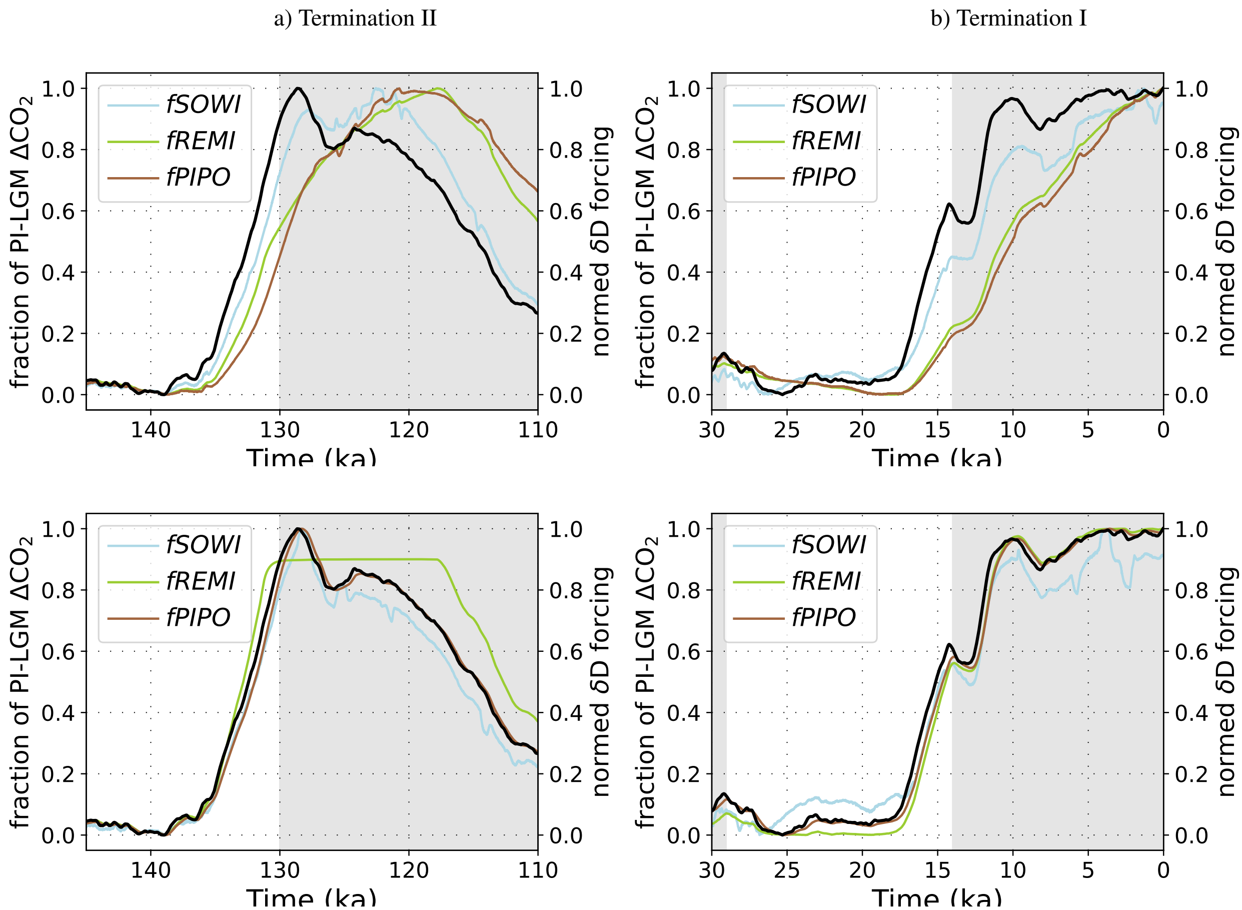

Figure S31. δD-derived scaling of the prescribed forcing and the resulting simulated atmospheric CO_2, normalized by the respective PI-LGM CO_2 difference, in selected simulations with interactive sediments (top row) and without interactive sediments (bottom row).